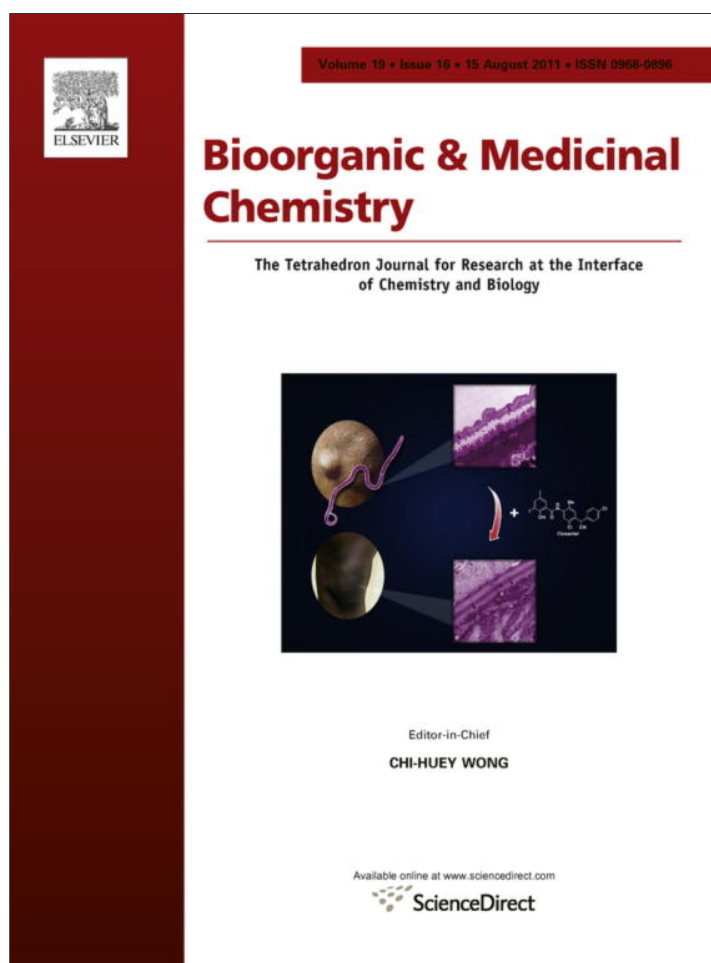


Provided for non-commercial research and education use.
Not for reproduction, distribution or commercial use.



This article appeared in a journal published by Elsevier. The attached copy is furnished to the author for internal non-commercial research and education use, including for instruction at the authors institution and sharing with colleagues.

Other uses, including reproduction and distribution, or selling or licensing copies, or posting to personal, institutional or third party websites are prohibited.

In most cases authors are permitted to post their version of the article (e.g. in Word or Tex form) to their personal website or institutional repository. Authors requiring further information regarding Elsevier's archiving and manuscript policies are encouraged to visit:

<http://www.elsevier.com/copyright>



Contents lists available at ScienceDirect

Bioorganic & Medicinal Chemistry

journal homepage: www.elsevier.com/locate/bmc

Ligand-based modelling followed by synthetic exploration unveil novel glycogen phosphorylase inhibitory leads

Maha Habash^a, Mutasem O. Taha^{b,*}^aDepartment of Pharmaceutical Chemistry and Pharmacognosy, Faculty of Pharmacy, Applied Science University, Amman, Jordan^bDrug Discovery Unit, Department of Pharmaceutical Sciences, Faculty of Pharmacy, University of Jordan, Amman, Jordan

ARTICLE INFO

Article history:

Received 19 May 2011

Revised 28 June 2011

Accepted 29 June 2011

Available online 7 July 2011

Keywords:

Glycogen phosphorylase

Pharmacophore

QSAR

In silico screening

In vitro validation

Synthetic exploration

ABSTRACT

Glycogen phosphorylase (GP) is a valid anti-diabetic target. Accordingly, we applied a drug discovery workflow to unveil novel inhibitory GP leads via combining pharmacophore modeling, QSAR analysis and in silico screening, followed by synthetic exploration of active hits. Virtual screening identified six low micromolar inhibitory leads from the National Cancer Institute (NCI) list of compounds. The most potent hits exhibited anti-GP IC₅₀ values of 3.2 and 4.1 μM. Synthetic exploration of hit **59** (IC₅₀ = 4.1 μM) yielded 25 lead inhibitors with the best illustrating IC₅₀ of 3.0 μM. Interestingly, we prepared several novel mixed oxalyl amide anti-GP leads employing new chemical reaction involving succinic acid-based adducts.

© 2011 Elsevier Ltd. All rights reserved.

1. Introduction

Glycogen phosphorylase (GP) plays key role in the regulation of blood glucose levels.^{1,2} Normally, GP mediates glycogenolysis, which contributes 40–50% of overnight glucose production. In type 2 diabetic patients, despite increased serum glucose levels, phosphorylase-mediated glycogenolysis continues to contribute 40–50% of overnight glucose production, increasing the problem of hyperglycemia.^{1,2}

GP catalyzes the hepatic glycogenolysis process by converting glycogen to glucose-1-phosphate, which is subsequently broken down by glucolysis into pyruvate that enters into citric acid cycle.³

In humans, there are three isozymes of GP named according to the tissues in which they are expressed: liver, muscle and brain. The muscle and brain isozymes that provide their specified tissues with its glucose demand, while the liver isozyme meets the glyce-mic demands of the body as a whole. Several published reports suggest that GP inhibition can lower blood glucose in diabetic models, thus promoting GP as a potential therapeutic target for treatment of type 2 diabetes.^{4,5}

GP contains at least six potential regulatory sites: (1) the Ser14-phosphate recognition site, (2) the catalytic site that binds glycogen and glucose-1-P as well as glucose and glucose analogues, (3) the AMP allosteric site, which binds AMP, IMP, ATP and

glucose-6-P, (4) the purine nucleoside site, which binds heterocyclic compounds such as caffeine and flavopiridol, (5) the glycogen storage site, and (6) the dimer interface site, which binds indole derivatives. Four of these sites are known to be inhibitor binding sites: the catalytic site, the AMP allosteric site, the inhibition site and the dimer interface site.⁵

GP exists in two interconvertible forms (**a** and **b**); the proportion of each form depends on the level of phosphorylation. The **b** form is transformed by phosphorylation into **a** form.^{2,5,6} GP_a, also known as relaxed state, has higher substrate affinity compared to GP_b (Tense state).^{3,7}

Inhibition of GP_a limits glycogen degradation and reduces hepatic glucose production, and therefore, should provide potential for the treatment of type 2 diabetes.⁷ Accordingly, GP inhibitors have received great recent interest as potential treatments for type 2 diabetes. For example, PSN-357 (Fig. 1) has been in phase I clinical trials since July 2005 as potential treatment for type 2 diabetes.⁹ Other interesting GP_a inhibitors were developed by major pharmaceutical companies, some of which are shown in Figure 2.³

The main focus of recent efforts towards the development of new GP_a inhibitors concentrate on structure-based ligand design,^{2,3,5,6,8,10,1c,69} 3D-QSAR studies (i.e., COMFA and COMSIA)^{10–12,14} and high throughput screening.¹³

To date, 22 human liver GP_a X-ray complexes are documented in the Protein Data Bank (PDB codes: 3DD1, 3DDS, 3DDW, 2ZB2, 3CEH, 3CEJ, 3CEM, 2QLL, 2ATI, 1WVO, 1EXV, 1EM6, 1L7X, 1L5R, 1WV1, 1WUY, 1WUT, 1XOI, 1L5Q, 1L5S, 1FCO and 1FA9 with resolution range: 1.80–3.3 Å). However, although considered the most

* Corresponding author. Tel.: +962 6 5355000x23305; fax: +962 6 5339649.

E-mail address: mutasem@ju.edu.jo (M.O. Taha).

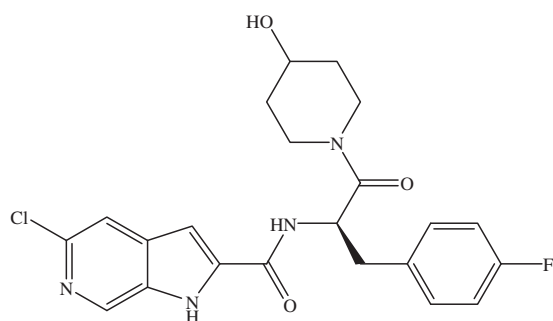


Figure 1. PSN-357 GPa inhibitor.

reliable structural information that can be used for drug design, crystallographic structures are limited by inadequate resolution¹⁵ and crystallization-related artifacts of the ligand–protein complex.^{16–18} Moreover, crystallographic structures generally ignore structural heterogeneity related to protein anisotropic motion and discrete conformational substrates.¹⁹

The continued interest in designing new GP inhibitors^{1c} combined with the drawbacks of structure-based design prompted us to explore the possibility of developing ligand-based three-dimensional (3D) pharmacophore(s) integrated within self-consistent QSAR model. This approach avoids the pitfalls of structure-based techniques; furthermore, the pharmacophore model(s) can be used as 3D search queries to discover new GP inhibitory scaffolds. We previously reported the use of this innovative approach towards the discovery of new inhibitory leads against glycogen synthase kinase-3,²⁰ bacterial MurF,²¹ protein tyrosine phosphatase,²² DPP IV,²³ hormone sensitive lipase,²⁴ β -secretase,²⁵ influenza neuraminidase,²⁶ cholesteryl ester transfer protein,²⁷ CDK1²⁸, β -D-galactosidase²⁹ and Heat Shock Protein 90a.³⁰

We employed the HYPOGEN module from the CATALYST software package to construct numerous reasonable binding hypotheses for GP inhibitors. Subsequently, genetic function algorithm (GFA) and multiple linear regression (MLR) analyses were employed to search for an optimal QSAR that combine high-quality binding pharmacophores with other molecular descriptors and capable of explaining bioactivity variation across a collection of GP inhibitors. The optimal pharmacophores were further validated

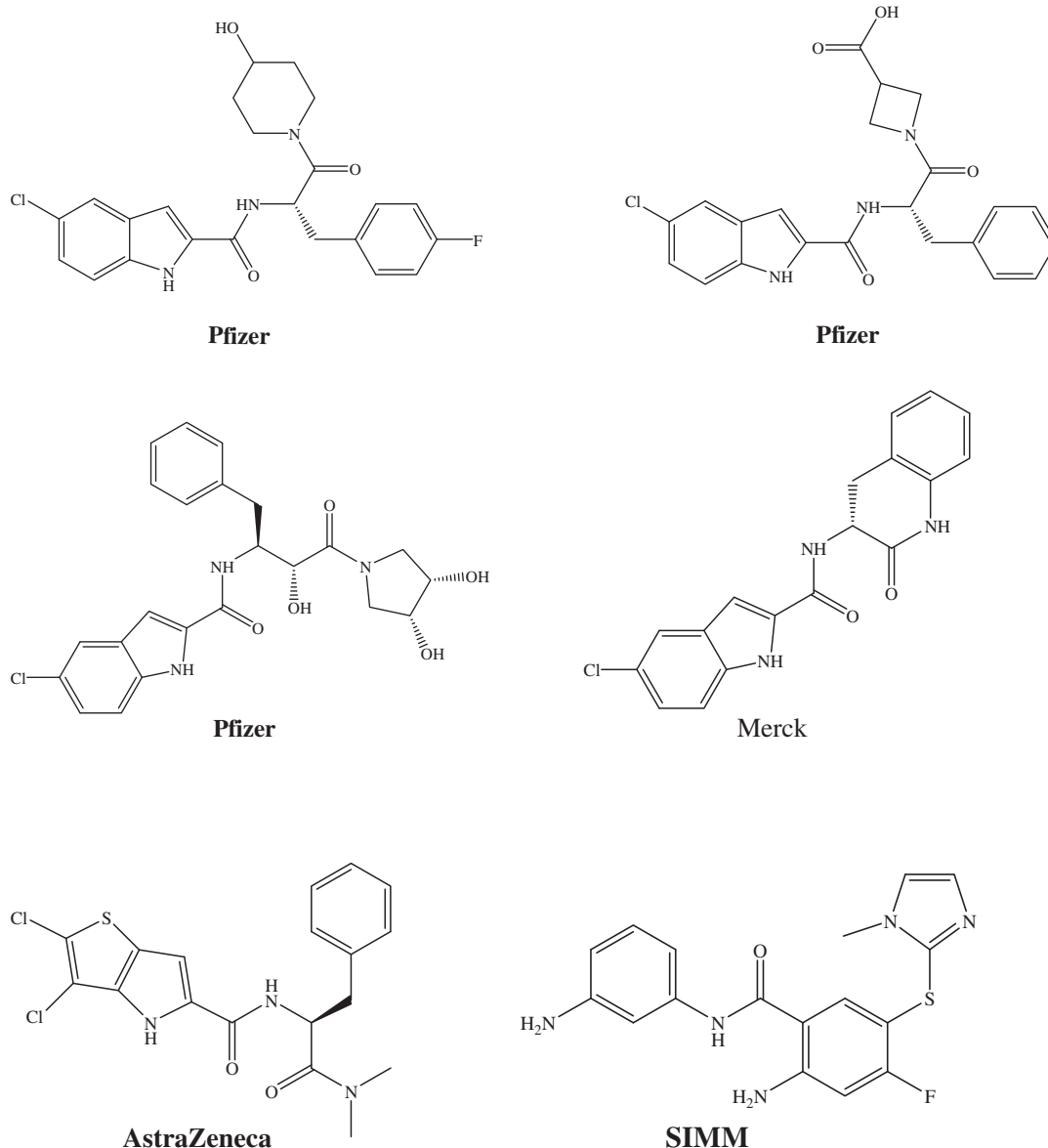


Figure 2. Some selected recently developed GPa inhibitors together with originating companies.³

by evaluating their abilities to successfully classify a list of compounds as active or inactive by assessing their receiver–operating characteristic (ROC) curves. The best pharmacophore was employed to screen the national cancer institute (NCI) list of compounds. One of the most active hits was used to guide the synthesis of two new series of potential GP α inhibitors based on oxalyl and malonyl scaffolds. Two of the synthesized compounds displayed low micromolar potencies.

CATALYST models drug–receptor interaction using information derived only from the drug structure. HYPOGEN identifies a 3D array of a maximum of five chemical features common to active training molecules, which provides a relative alignment for each input molecule consistent with their binding to a proposed common receptor site. The chemical features considered can be hydrogen bond donors and acceptors (HBD and HBA), aliphatic and aromatic hydrophobes (Hbic), positive and negative ionizable (Poslon and Neglon) groups and aromatic planes (RingArom). The conformational flexibility of training ligands is modeled by creating multiple conformers, judiciously prepared to emphasize representative coverage over a specified energy range. CATALYST pharmacophores have been used as 3D queries for database searching and in 3D-QSAR studies.^{21,31–33}

2. Results and discussion

CATALYST-based automatic pharmacophore construction was performed using a collection of molecules with biological activities ranging from 3.5 to 4.0 logarithmic. CATALYST pharmacophores (hypotheses) explain the variability of activity of the molecules with respect to the geometric localization of the chemical features present in the molecules used to build it. Different hypotheses were generated for a series of GP inhibitors. A total of 37 compounds were used in this study (1–37, Table S1 in Supplementary data). Three training subsets were selected from the collection (Table 1). Genetic algorithm and multiple linear regression statistical analysis were subsequently employed to select an optimal combination of complementary pharmacophores capable of explaining bioactivity variations among all inhibitors. Bioactive hits were used to guide synthetic exploration for new GP inhibitors.

2.1. Data mining and conformational coverage

The literature was extensively surveyed to identify as many reported structurally diverse GP inhibitors as possible. A dataset of 37 dihydroquinolinones (1–37, Table S1 in Supplementary data) was used for pharmacophore modeling and subsequent QSAR analysis (1–37, see Table S1 in Supplementary data). However, we were forced to select this relatively limited list of compounds because they satisfied two important prerequisites for pharmacophore and QSAR modeling: (i) they were all bioassayed by a single procedure. Consistency in bioassay is a major requirement for QSAR modeling as it is not possible to model bioactivity data generated via more than one bioassay procedure. (ii) They exhibit wide bioactivity range, that is, over 4 logarithmic cycles.

The 2D structures of the inhibitors were imported into CATALYST and converted automatically into plausible 3D single conformer representations. The resulting single conformer 3D structures were

used as starting points for conformational analysis and in the determination of various molecular descriptors for QSAR modeling.

The conformational space of each inhibitor was extensively sampled utilizing the poling algorithm employed within the CONFIRM module of CATALYST.³⁵ Conformational coverage was performed employing the ‘Best’ module to ensure extensive sampling of conformational space. Efficient conformational coverage guarantees minimum conformation-related noise during pharmacophore generation and validation stages. Pharmacophore generation and pharmacophore-based search procedures are known for their sensitivity to inadequate conformational sampling within the training compounds.³⁶

2.2. Exploration of GP pharmacophoric space

CATALYST-HYPOGEN enables automatic pharmacophore construction by using a collection of at least 16 molecules with bioactivities spanning over 3.5 orders of magnitude.^{37–42}

Accordingly, since we have a list of 37 GP inhibitors of evenly spread bioactivities over several orders of magnitude, we were prompted to employ HYPOGEN to identify possible pharmacophoric binding modes assumed by GP inhibitors within their corresponding GP binding site (see Section S1 in Supplementary data).³⁹

It was decided to explore the pharmacophoric space of GP inhibitors under reasonably imposed ‘boundaries’ through twelve HYPOGEN automatic runs (Table S2 in Supplementary data) and employing three carefully selected training subsets (i.e., from the collected compounds): subsets I, II and III, shown in Table 1. The training compounds in these subsets were selected in such a way to guarantee maximal 3D diversity and continuous bioactivity spread over more than 3.5 logarithmic cycles. Furthermore, the training inhibitors were selected in such a way that differences in their anti-GP bioactivities are primarily attributable to the presence or absence of pharmacophoric features (e.g., HBA or HBD or hydrophobic or Ring Aromatic) rather than steric shielding and/or bioactivity-enhancing or -reducing auxiliary groups (e.g., electron donating or withdrawing groups). Special emphasis was given to the 3D diversity of the most active compounds in each training subset (Table 1) because these have significant influence on the extent of the evaluated pharmacophore space via the Constructive Phase of HYPOGEN algorithm (see Section S1 in Supplementary data).

Guided by our reasonably restricted pharmacophoric exploration concept, the software was restricted to explore pharmacophoric models incorporating from zero to three features of selected feature types (i.e., HBA, HBD, hydrophobic and Ring Aromatic), that is, instead of the default range of zero to five. Furthermore, to further limit the investigated pharmacophoric space, only four and five-featured pharmacophores were explored. Three- and two-featured pharmacophores are rather promiscuous as 3D search queries and not adequate descriptions of ligand–GP binding. Table S2 (in Supplementary data) shows the training sets and CATALYST run parameters employed in exploring GP pharmacophoric space.

In each run, the resulting binding hypotheses were automatically ranked according to their corresponding ‘total cost’ value: defined as the sum of error cost, weight cost and configuration cost

Table 1
Training subsets employed in exploring the pharmacophoric space of GP inhibitors, numbers correspond to compounds in Table S1 in Supplementary data

Training set	Most active subset ^a	Intermediate subset	Least active subset ^b	No. of compounds
I	7, 13, 15, 17, 31, 32, 33, 37	2, 12, 18, 19, 28	22, 25, 29	16
II	4, 7, 9, 17, 24, 31, 36, 37	1, 2, 8, 12, 14, 21	22, 25	16
III	4, 7, 9, 17, 24, 31, 32, 37	1, 2, 12, 14, 18, 19, 21, 28	22, 25, 29	20

^a Potency categories as defined by Eq. S1 in Supplementary data.

^b Potency categories as defined by Eq. S2 in Supplementary data.

(see Section S2 in Supplementary data). Error cost provides the highest contribution to total cost and it is directly related to the capacity of the particular pharmacophore as 3D-QSAR model, that is, in correlating the molecular structures to the corresponding biological responses. HYPOGEN also calculates the cost of the null hypothesis, which presumes that there is no relationship in the data and that experimental activities are normally distributed about their mean. Accordingly, the greater the difference from the null hypothesis cost (residual cost, Table 2), the more likely that the hypothesis does not reflect chance correlation.^{37–42} Table 2 summarizes the pharmacophoric features and success criteria of best GP representative hypotheses (see Section S2 in Supplementary data).

Eventually, 120 pharmacophore models emerged from 12 automatic HYPOGEN runs, out of which 84 models illustrated confidence levels $\geq 85\%$ (based on Fisher's randomization test).^{43,61} These successful models were clustered and the best representatives (28 models) were used in subsequent QSAR modeling, as in Table 2.

Clearly from Table 2, all representative models shared comparable features and acceptable statistical success criteria. Emergence of several comparable pharmacophore models suggests the ability of GP ligands to assume multiple pharmacophoric binding modes within the binding pocket. Therefore, it is quite challenging to select any particular pharmacophore hypothesis to represent the binding process.

2.3. QSAR modeling

Pharmacophoric hypotheses are important tools in drug design and discovery as they provide excellent insights into ligand-macromolecule recognition. Moreover, they can be used as 3D search queries to mine for new biologically interesting scaffolds. However, their predictive value as 3D-QSAR models is usually limited by steric shielding and bioactivity-enhancing or -reducing auxiliary groups.⁴² This point combined with the fact that pharmacophore modeling of GP inhibitors furnished several binding hypotheses of comparable statistical criteria (Table 2) prompted us to employ classical QSAR analysis to search for the best combination of pharmacophore(s) and other 2D descriptors capable of explaining bioactivity variation across the whole list of collected inhibitors (1–37, Table S1 in Supplementary data). Genetic function approximation and multiple linear regression QSAR (GFA-MLR-QSAR) analysis were employed to search for an optimal QSAR equation(s).

GFA-MLR-QSAR selects optimal descriptor combinations based on the Darwinian concept of genetic evolution whereby the statistical criteria of regression models from different descriptor combinations (chromosomes) are employed as fitness criteria.⁴⁴ GFA-MLR-QSAR analysis was employed to explore various combinations of pharmacophores and other structural descriptors and to evaluate their statistical properties as predictive QSAR models.

The fit values obtained by mapping the 28 representative hypotheses against all collected GP inhibitors (1–37, Table S1 in Supplementary data) were enrolled as independent variables (genes) in a cycle of GFA-MLR-QSAR analysis over 30,000 iterations employing Friedman's LOF fitness criterion (see Section 4.1.3).^{37,45} However, since it is essential to access the predictive power of the resulting QSAR models on an external set of inhibitors, 7 molecules were randomly selected and used as external test molecules for validating the QSAR models (Table S1 in Supplementary data, see Section 4.1.3). Moreover, all QSAR models were cross-validated automatically using the leave-one-out cross-validation in CERIU2.^{37,45}

Equation 1 shows the details of the optimal QSAR model. Figure 3 shows the corresponding scatter plots of experimental versus estimated bioactivities for the training and testing inhibitors.

$$\begin{aligned} \text{Log}(1/IC_{50}) &= 6.27 + 0.22(\text{Hypo12/7}) - 0.20\text{log}(Z) 1.35\kappa_2^2 \\ r_{30}^2 &= 0.69, F\text{-statistic} = 18.70, r_{BS}^2 = 0.69, r_{LOO}^2 = 0.58, r_{PRESS(7)}^2 = 0.91 \end{aligned} \quad (1)$$

where r_{30}^2 is the correlation coefficient, F is Fisher statistic, n is the number of observations, r_{BS}^2 is the bootstrapping regression coefficient, r_{LOO}^2 is the leave-one-out correlation coefficient and r_{PRESS}^2 is the predictive r^2 determined for 7 randomly selected test compounds.^{37,45} $\text{Log}(Z)$ is natural logarithm of Hosoya connectivity index, while κ_2^2 is the second order Kier's alpha-modified shape index.⁴⁴ Hypo12/7 represents the fit values of the training compounds against the 7th pharmacophore model generated in the 12th modeling runs, as in Tables 3 and 4. Figure 4 shows Hypo12/7 and how it maps the most potent training inhibitor **9** ($IC_{50} = 25$ nM), while Table S3 (in Supplementary data) shows the X , Y , and Z coordinates of the Hypo12/7.

Emergence of connectivity and shape indices in Eq. 1 illustrates certain role played by the ligands' topology in the binding process. However, despite their predictive significance, their information content is quite obscure.

On the other hand, emergence of Hypo12/7 in QSAR Eq. 1 suggests the existence of a single corresponding binding mode assumed by inhibitors within the binding pocket of GP. To further validate this conclusion we compared this binding model with the bound conformation of the co-crystallized ligand CP-403700 within GP (PDB code: 1L5R, resolution 2.1 Å).

Figure 5 shows the chemical structure of CP-403700 and compares its GP complex with the way it maps Hypo12/7 employing rigid mapping, that is, by fitting the ligand's bound state against corresponding pharmacophore without conformational adjustments. Fitting the carboxylate fragment of CP-403700 against HBA feature in Hypo12/7 (Fig. 5b) corresponds to hydrogen-bonding interaction connecting this fragment with H₂O481, which is in turn hydrogen-bonded to phenolic hydroxyl of Tyr226, as in Figure 5a. Similarly, fitting one of the ligand's carbonyls against a HBA feature in Hypo12/7 corresponds to hydrogen-bonding interaction connecting the same carbonyl with the ammonium side chain of Lys191 (Fig. 5a and b). While, mapping the benzyl ring of CP-403700 against Hbc feature in Hypo12/7 (Fig. 5b) correlates with placing this ring in a hydrophobic pocket comprised of the side chains of His57, Phe53 and Pro188. On the other hand, mapping of the chlorinated indole ring of CP-403700 ligand against two hydrophobic features in Hypo12/7 (Fig. 5b) agrees with positioning this fragment in a hydrophobic pouch consisting of the side chains of Trp67, Val40, Val64, Pro229 and the butylenes linker of Lys191 and (Fig. 5a).

Clearly from the above discussion, Hypo12/7 represents a valid binding mode assumed by ligand within GP. Furthermore, this model points to limited number of critical interactions required for high ligand-GP affinity in the binding mode. In contrast, crystallographic complexes reveal many bonding interactions without highlighting critical ones. Incidentally, Figure 5a only shows interactions corresponding to pharmacophoric features while other binding interactions were hidden for clarity.

2.4. Addition of exclusion volumes

Although ligand-based pharmacophores serve as excellent tools to probe ligand/macromolecule recognition and can serve as useful 3D-QSAR models and 3D search queries, they suffer from a major drawback: They lack steric constraints necessary to define the size of the binding pocket. This liability might render pharmacophoric models promiscuous. Therefore, we decided to complement our QSAR-selected pharmacophore with exclusion spheres employing HipHop-Refine module within CATALYST. Excluded volumes

Table 2
The success criteria of representative GP pharmacophore hypotheses

Training Set ^a	Run ^b	Hypotheses ^c	Pharmacophoric features in generated hypotheses	Total cost	Config cost	Cost of null hypothesis	Residual cost ^d	R ^e	F-Statistic ^f	Cat-scramble (%) ^g	
I	1	2	HBA, 3×Hbic, 5×EV	73.9	15.8	100.9	27.0	0.98	26.9	85	
		3	HBA, 3×Hbic, RingArom, 6×EV	75.4	15.8	100.9	25.5	0.98	2.9	85	
		6	HBA, 3×Hbic, RingArom, 5×EV	80.9	15.8	100.9	20.0	0.88	19.2	95	
		8	HBD, 3×Hbic, 3×EV	81.3	15.8	100.9	19.6	0.90	34.7	95	
		9	HBD, HBA, 3×Hbic, 1×EV	81.6	15.8	100.9	19.3	0.91	26.6	95	
	2	2	HBD, 2×Hbic, RingArom, 9×EV	73.6	14.1	100.9	27.3	0.96	4.9	85	
		3	HBD, 2×Hbic, RingArom, 5×EV	79.1	14.1	100.9	21.8	0.92	1.3	85	
		4	HBA, 2×Hbic, RingArom, 7×EV	79.4	14.1	100.9	21.5	0.91	1.8	85	
		5	HBA, 3×Hbic, 5×EV	80.6	14.1	100.9	20.3	0.94	17.1	85	
		7	HBA, 2×Hbic, RingArom, 8×EV	81.5	14.1	100.9	19.4	0.86	1.3	85	
II	5	2	HBD, 2×Hbic, RingArom, 5×EV	75.6	15.8	94.6	19.0	0.94	9.3	95	
		3	HBD, 3×Hbic, 5×EV	76.5	15.8	94.6	14.1	0.93	8.7	85	
	6	2	HBD, 2×Hbic, RingArom,	76.4	14.0	94.6	18.0	0.92	4.3	95	
		6	2HBA, 2×Hbic	79.5	14.0	94.6	15.1	0.87	5.1	85	
		7	HBD, HBA, Hbic, RingArom	79.5	14.0	94.6	15.1	0.87	2.2	85	
		10	HBD, HBA, 2 Hbic	79.9	14.0	94.6	14.7	0.86	6.6	85	
	7	3	HBD, 3×Hbic, RingArom, 6×EV	73.6	13.2	94.6	21.0	0.93	3.5	90	
	III	9	1	2×HBD, 3×Hbic, 7×EV	90.4	15.8	120.9	30.5	0.94	2.1	85
			8	HBD, 3×Hbic, RingArom, 6×EV	101	15.8	120.9	19.9	0.83	15.7	95
			10	3×Hbic, RingArom, 4×EV	102	15.8	120.9	18.9	0.82	5.6	95
10		1	HBD, Hbic, 2× RingArom, 7×EV	88.9	14.02	120.9	32.0	0.94	1.9	85	
		4	HBA, 3×Hbic	99.9	14.02	120.9	21.0	0.83	6.7	90	
		8	2× HBD, Hbic, RingArom, 4×EV	102.1	14.02	120.9	18.8	0.81	0.0	90	
		9	2× HBA, Hbic, RingArom, 6×EV	102.4	14.02	120.9	18.5	0.80	2.0	90	
		11	9	2HBA, 3×Hbic, 4×EV	97.1	13.3	120.9	23.8	0.85	5.2	95
12		6	HBD, HBA, 3×Hbic, 3×EV	91.4	10.124	120.9	29.5	0.88	2.1	95	
		7 ^h	2HBA, 3×Hbic, 3×EV	92.1	10.124	120.9	28.8	0.87	4.5	95	

^a Training sets as in Table 1.

^b Run number as in Table S2 in Supplementary data.

^c Serial numbers given by CATALYST for individual hypotheses and reported in the log book of the corresponding automatic run.

^d The difference between the total cost and the cost of the corresponding null hypotheses.

^e Correlation coefficient for given by CATALYST for individual hypotheses against the particular training subset only.

^f Fisher-statistic calculated from the correlation between pharmacophore-based bioactivity estimates (calculated from Eqs. S1 and S2 in Supplementary data) against the bioactivities of all collected compounds.

^g Fisher confidence level calculated employing the cat. scramble methods (see Section S2 in Supplementary data).

^h This pharmacophore appeared in the best QSAR equation (bolded).

resemble sterically inaccessible regions within the binding site.^{20–22,24,28,32,37,46}

HipHop-Refine requires a list of training compounds together with two qualitative descriptors that characterize the way by which each training compound contributes in defining the exclusion space, that is, Principal and MaxOmitFeat (see Section S3 in Supplementary data for more details). Table S4 (in Supplementary data) lists the collected compounds together with their HipHop-Refine parameters. Figure 4c and d show the sterically-refined version of Hypo12/7 (32 added exclusion volumes) and how it maps 9 (IC₅₀ = 25 nM).

2.5. Receiver operating characteristic (ROC) curve analysis and shape constraints

To further validate the resulting models (both QSAR and pharmacophore), we subjected Hypo12/7 to receiver-operating curve (ROC) analysis. In ROC analysis, the ability of a particular pharmacophore model to correctly classify a list of compounds as actives and inactives is indicated by the area under the curve (AUC) of the corresponding ROC in addition to other parameters, namely, overall accuracy, overall specificity, overall true positive rate and overall false negative rate (see Section 4.1.4 for more details). Table S5 (in Supplementary data) and Figure 6 show the ROC results of Hypo12/7, as well as its sterically-refined version.

Clearly from the Figure 6 and Table S5 (in Supplementary data), steric refinement significantly improved the performance of Hypo12/7 as reflected by ROC-AUC values, which shifted from 70% to 90% upon addition of exclusion spheres. Nevertheless, steric

refinement undermined the true positive rate (TPR) by ca. 25%, which suggest that although steric-refinement improved the classification power of the pharmacophore (AUC), it caused some loss in the number of captured active hits (true positives). This might be because exclusion volumes impose strict restrictions on captured hits causing the pharmacophore to inappropriately miss some active hits.

2.6. In silico screening of databases

Sterically-refined Hypo12/7 was used as 3D search query against the national cancer institute list of compounds (NCI, includes 238,819 compounds).³⁶ Hits are defined as those compounds that have their chemical moieties spatially overlap (map) with corresponding features in the pharmacophoric query. The search culminated in 7739 hits that were subsequently filtered based on Lipinski's⁴⁷ and Veber's rules⁴⁸ to yield 146 drug-like hits.

Surviving hits were fitted against Hypo12/7 (see the fit Eq. 6 under Experimental) and their fit values were substituted in QSAR Eq. 1 to determine their predicted bioactivities. However, in order to minimize the impact of any possible extrapolatory QSAR-based prediction errors on decisions regarding which hits merit subsequent in vitro testing, Log (1/IC₅₀) predictions were employed merely to rank the corresponding hits. Subsequently, the highest ranking 52 hits were acquired for in vitro evaluation. Table 3 shows the highest ranking hits (48–99) based on QSAR Eq. 1, their QSAR-based predictions, as well as their experimental in vitro anti-GP bioactivities.

The tested hits illustrated diverse in vitro activities against GP_A ranging from zero to 65% inhibition at 10 μM concentrations.

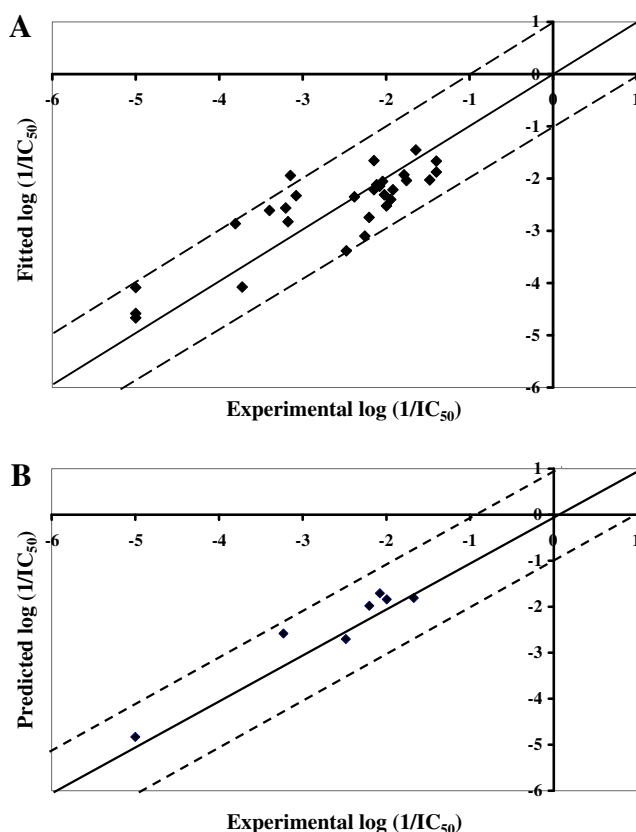


Figure 3. Experimental versus fitted (A, 30 compounds, $r_{LOO}^2 = 0.583$) and predicted (B, 7 compounds, $r_{PRESS}^2 = 0.907$) bioactivities calculated from the best QSAR model (Eq. 1). The solid lines are the regression lines for the fitted and predicted bioactivities of training and test compounds, respectively, whereas the dotted lines indicate the 1.0 log point error margins.

However, six hits achieved $\geq 40\%$ GPa inhibition at $10 \mu\text{M}$ concentration prompting subsequent assessment of their IC_{50} values against GPa. Figure S1 (in Supplementary data) shows the dose–inhibition plots of hit compounds.

Clearly from Table 3 and Figure S1 (in Supplementary data) that there is significant deviation between QSAR-predicted bioactivities and experimentally determined IC_{50} values. This is not unexpected as there is significant structural dissimilarity between training compounds and hits (see Section 2.8). Furthermore, the number of training compounds is rather limited to allow effective pharmacophore and QSAR analysis (only 37 compounds, Table S1 in Supplementary data). Both factors seem to explain the difference between predicted and experimental inhibitory profiles of captured hits. Nevertheless, hit **59** (Table 3) exhibited the closest predicted-to-experimental IC_{50} difference, suggesting that QSAR equation 1 and the associated pharmacophore model (Hypo12/7) exhibit optimal predictive potential for this scaffold, which together with its superior anti-GPa IC_{50} ($4.1 \mu\text{M}$), prompted us to use this structure as guide for subsequent synthetic exploration towards more potent GPa inhibitors.

2.7. Synthesis and bioactivities of pharmacophore-guided GP Inhibitors

The facts that Hypo12/7 exhibited two adjacent HBA features combined with the presence of two adjacent amidic carbonyls in potent training compounds (e.g., **9**, see Fig. 4) and in the well-predicted potent NCI hit **59** prompted us to synthetically explore several diverse oxalyl and malonyl diamides as potential inhibitors

of GPa. It was hypothesized that introducing two well-positioned central HBA features separating a two aromatic ring-based scaffold should maximize ligand–GPa binding by allowing the ligands to tightly map Hypo12/7.

Accordingly, we prepared several malonyl- and oxalyl-diamide products by reaction of some selected aromatic amines with malonyl dichloride, or succinic anhydride/oxalyl chloride mixture, respectively, as in Schemes 1 and 2. The aromatic amines were selected in such a way to maximize electronic and steric diversity among prepared compounds, that is, the aromatic substituents ranged from electron donating (e.g., methyl, aromatic rings, methoxy groups) to electron withdrawing groups (e.g., chloro), and from small substituents (e.g., methylbenzene) to fairly large groups (e.g., naphthyl), as can be seen in Table 4. However, it must be mentioned that we failed to access any nitro-substituted derivatives probably because of the weak nucleophilic properties of nitro-substituted aromatic amines.

Although the preparation procedure of the malonyl derivatives is well known, that is, through nucleophilic amine attack on malonyl dichloride (Scheme 1),⁴⁹ our synthetic approach to the oxalyl diamides is completely novel. In this approach, succinic anhydride was employed as amine donor to allow mono-substitution of the oxalyl chloride as shown in Scheme 2. Scheme 3 shows the proposed mechanism of this approach: the mixed anhydride intermediate of succiniamide (**A** in Scheme 3) undergoes azalactonization reaction to yield cyclic isoimide intermediate (**B** in Scheme 3) in a similar fashion to that reported by Gerhard and Rene⁵⁰ albeit mediated by oxalylchloride instead of perchloric acid. Subsequently, the isoimide intermediate (**B** in Scheme 3) apparently acts as imine nucleophile and attacks a second oxalyl-chloride molecule to form isoimidium-oxalylchloride adduct (**C** in Scheme 3). Apparently, intermediate **C** (in Scheme 3) is immune to second nucleophilic attacks by isoimide **B** (in Scheme 3), that is, to yield symmetrical oxalamides, probably because (i) imine nitrogens of intermediate **B** are weak nucleophiles due to their sp^2 hybridization and the steric bulk of isoimide, and (ii) stabilization of the anti-bonding orbital (LUMO) of the acyl chloride carbon by the electronic density donated from the lone pair of electrons of the cyclic isoimide oxygen, as in Figure 7.

However, the isoimidium intermediate (**C**) seems to readily undergo nucleophilic attacks by the added aromatic amines to yield isoimidium-oxalyl-amide adducts (intermediate **D** in Scheme 3), which is hydrolyzed to oxalyl diamide products and succinic anhydride. Interestingly, similar *N*-phenyl-isoimides were reported to act as amine donors to aldehydes leading to imines.⁵⁰

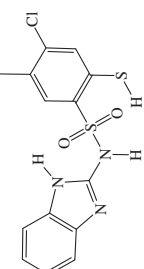
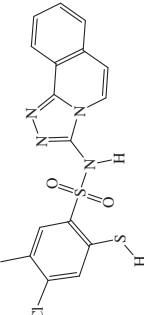
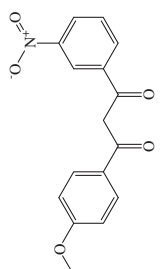
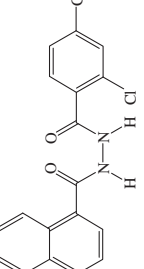
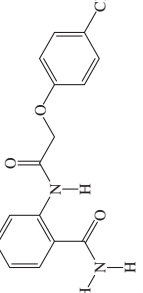
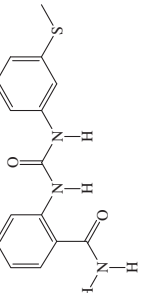
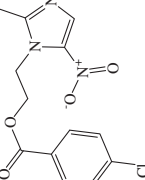
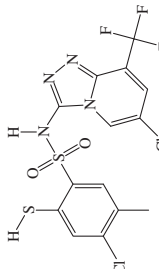
Upon evaluating the resulting oxalyl- and malonyl-diamides against GPa at $10 \mu\text{M}$ concentrations, they show diverse anti-GPa bioactivities. Table 4 shows the synthesized compounds (**100–111**, **120–132**), their QSAR-based predictions and experimental IC_{50} values.

Clearly from Table 4, a significant difference is seen between predicted IC_{50} values of prepared compounds and their experimental bioactivities. Probably, this behavior is due to the significant physicochemical differences between training and prepared compounds (see Section 2.8).

Surprisingly, although **120** and **131** failed to fully fit Hypo12/7 (see Figs. 9b and 8b), they illustrated comparatively significant anti-GPa IC_{50} values, that is, 5 and 3 μM , respectively. In the case of **131**, this behavior is probably explainable by the existence of an additional interaction within the **131**–GPa complex extra to those suggested in Hypo12/7. To probe this point further, we docked **131** into the binding pocket of the GPa (PDB code 1L5R, Resolution = 2.1 Å) employing Ligandfit docking engine and consensus scoring based on 6 docking-scoring functions, namely, JAIN,⁵¹ LigScore1, LigScore2,^{52,53} PLP1,⁵⁴ PLP2⁵⁵ and PMF.^{56–58} Figure 8a shows the highest-ranking docked pose of **131** in GPa compared with

Table 3
 In silico hits, their fit values against (Hypo12/7), corresponding QSAR estimates from Eq. 1 and in vitro anti-GP bioactivities

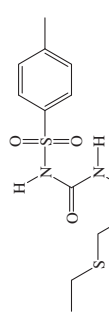
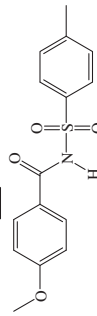
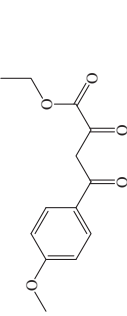
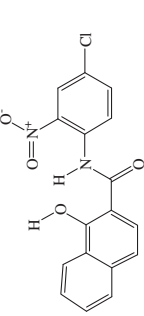
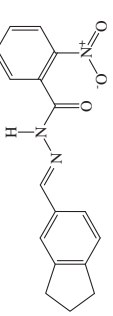
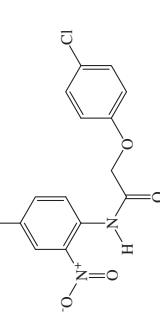
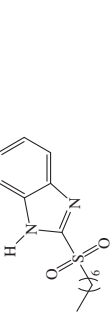
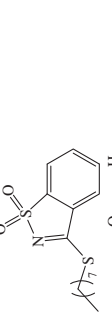
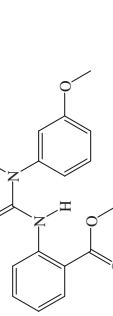
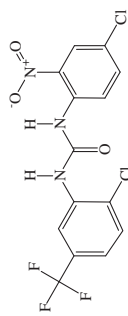
Hit Compound	NCI code	Structure	Fit value against Hypo12/7 ^a	QSAR Predictions		Experimental	
				Log (1/IC ₅₀)	IC ₅₀ (μM)	% Inhibition at 10 μM ^b	IC ₅₀ (μM) ^b
48	NSC90313		5.4	-1.847	0.07	65	3.2
49	NSC174281		4.8	-3.738	5.47	30	ND ^c
50	NSC280876		9.0	-1.511	0.03	49	16.5
51	NSC404052		6.6	-1.626	0.04	32	ND ^c
52	NSC682567		6.9	-3.112	1.29	24	ND ^c
53	NSC66430		3.7	-1.995	0.10	27	ND ^c
54	NSC176370		7.7	-1.475	0.03	24	ND ^c
55	NSC195114		7.5	-2.4	0.25	23	ND ^c
56	NSC27175		6.2	-0.696	0.01	29	ND ^c

57	NSC681174		4.6	-2.087	0.12	45	6.9
58	NSC686774		7.9	-2.687	0.49	42	7.5
59	NSC61623		9.3	-2.966	0.92	60	4.1
60	NSC88165		8.1	-3.574	3.75	39	ND ^c
61	NSC164459		8.6	-3.083	1.21	38	ND ^c
62	NSC216623		9.1	-2.754	0.57	36	ND ^c
63	NSC302323		8.7	-2.633	0.43	32	ND ^c
64	NSC673994		9.2	-3.127	1.34	53	5.9

(continued on next page)

Table 3 (continued)

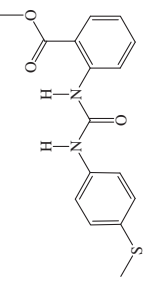
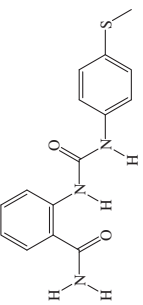
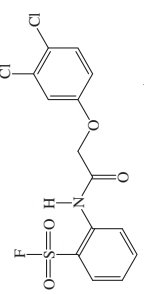
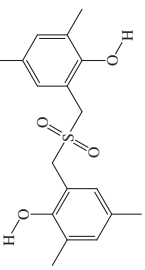
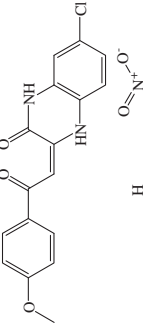
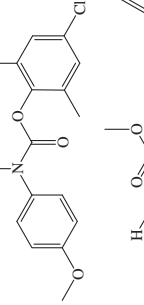
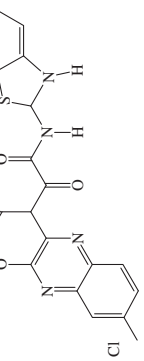
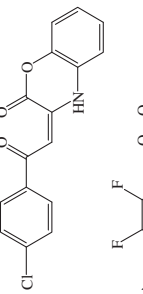
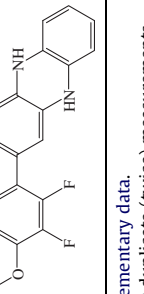
Hit Compound	NCI code	Structure	Fit value against Hypo12/7 ^a	QSAR Predictions		Experimental	
				Log (1/IC ₅₀)	IC ₅₀ (μM)	% Inhibition at 10 μM ^b	IC ₅₀ (μM) ^b
65	NSC11437		8.8	-2.603	0.40	25	ND ^c
66	NSC16743		9.0	-3.316	2.07	8.0	ND ^c
67	NSC29159		8.8	-4.003	10.07	3	ND ^c
68	NSC50690		9.8	-2.693	0.49	22	ND ^c
69	NSC58325		10.3	-4.075	11.89	26	ND ^c
70	NSC88898		9.5	-4.323	21.04	11	ND ^c
71	NSC134224		9.4	-2.721	0.53	34	ND ^c
72	NSC141980		10.3	-3.159	1.44	15	ND ^c

73	NSC141981		10.4	-3.134	1.36	9.0	ND ^c
74	NSC144076		9.8	-1.693	0.05	18	ND ^c
75	NSC146837		9.4	-2.472	0.30	34	ND ^c
76	NSC151098		8.00	-2.838	0.69	25	ND ^c
77	NSC157495		7.9	-2.97	0.93	17	ND ^c
78	NSC164588		8.8	-3.442	2.77	25	ND ^c
79	NSC191949		8.5	-1.99	0.10	12	ND ^c
80	NSC202468		10.0	-3.018	1.04	2.0	ND ^c
81	NSC203848		8.7	-3.814	6.52	12	ND ^c
82	NSC203972		8.4	-3.928	8.47	18	ND ^c

(continued on next page)

Table 3 (continued)

Hit Compound	NCI code	Structure	Fit value against Hypo12/7 ^a	QSAR Predictions		Experimental	
				Log (1/IC ₅₀)	IC ₅₀ (μM)	% Inhibition at 10 μM ^b	IC ₅₀ (μM) ^b
83	NSC204090		8.8	-3.329	2.13	7.0	ND ^c
84	NSC204442		8.3	-2.986	0.97	17	ND ^c
85	NSC205486		9.6	-3.768	5.86	7.0	ND ^c
86	NSC205499		8.0	-2.848	0.70	26	ND ^c
87	NSC205520		9.3	-3.757	5.71	9.0	ND ^c
88	NSC205686		10.4	-3.067	1.17	9.0	ND ^c
89	NSC205703		10.7	-3.094	1.24	16	ND ^c
90	NSC205705		8.6	-2.055	0.11	21	ND ^c

91	NSC205797		8.7	-4.056	11.38	7.0	ND ^c
92	NSC205827		9.1	-2.765	0.58	17	ND ^c
93	NSC211982		9.1	-3.633	4.30	16	ND ^c
94	NSC280880		8.5	-2.585	0.38	20	ND ^c
95	NSC370919		8.9	-2.395	0.25	24	ND ^c
96	NSC379459		9.7	-3.570	3.72	32	ND ^c
97	NSC648606		10.7	-3.209	1.62	34	ND ^c
98	NSC682580		8.3	-1.374	0.02	26	ND ^c
99	NSC658713		9.6	-2.972	0.94	15	ND ^c

^a Best-fit values calculated by Eq. S2 in Supplementary data.

^b Bioactivity values are the average of at least duplicate (twice) measurements

^c ND: not determined

mapping **131** against Hypo12/7. Clearly, mapping the two carbonyls of **131** against two HBA features in Hypo12/7 agrees with hydrogen-bonding interactions connecting the two groups with the guanidine of Arg60 and ammonium of Lys191. In fact, the later interaction is reinforced by a network of hydrogen bonds involving H₂O34 and the peptidic NH of Ser192. Similarly, mapping the benzylic ring against a hydrophobic feature in Hypo12/7 agrees with positioning this group into a hydrophobic pocket comprised of the side chains of Trp67, Pro229 and Val64 (Fig. 8a). Similarly, mapping the chlorophenyl group against a hydrophobic feature in Hypo12/7 corresponds to hydrophobic stacking involving this group and the aromatic ring of Phe53.

However, clearly from Figure 8b, **131** misses one hydrophobic feature in Hypo12/7 corresponding to interaction with Val64 (see Fig. 5). Still, the close proximity of the *o*-chloro substituent in **131** to H₂O34 suggests it is involved in electrostatic and hydrogen-bonding interactions with this water molecule, which is pinned by hydrogen-bonding interactions with the peptidic NH of Ser192. This extra interaction probably compensates for the lost hydrophobic feature in Hypo12/7.

Likewise, **120** seems to dock into GP_a in a similar manner to the way it maps Hypo12/7 (see Fig. 9): fitting the two central HBAs against the oxalyl carbonyls correspond to hydrogen-bonding interactions connecting these carbonyls with the side chains of Lys192 and Arg60, as in Figure 9. On the other hand, fitting the aromatic methyls against two hydrophobic features agrees with docking these methyls into hydrophobic pockets comprised of the side chains of Val40, Val64 and Leu39. Nevertheless, the same set of interactions can be also noticed in the docked complexes of other oxalamides despite their inferior bioactivities, for example, **124**, **126** and **132**. We believe that the superior bioactivity of **120** is related to the close analogy between its bound conformer and the lowest energy conformer of its unbound structure. The two *ortho*-methyl groups force the phenyl substituents to assume perpendicular conformation to that of the oxalamide linker in the unbound structure, which is although electronically disfavoured because it breaks the electronic delocalization of the two phenyl groups across the oxalamide linker, it closely resembles the docked conformer of **120** (see Fig. 9). This suggests that **120**–GP_a binding requires minimal energy expenditure to strain **120** within the binding pocket, which is apparently not the case in the less potent oxalamides. In other words, the energy difference between unbound conformers and bound counterparts is rather significant in poorly-potent oxalamides suggesting significant energetic cost in straining the ligand molecules to fit within the binding site. This should reduce the free energy gains of binding explaining the apparent reduction in bioactivity of poorly potent oxalamide analogues despite their theoretically tight fit against Hypo12/7, for example, **121**, **122** and **130** (see Fig. 10).

2.8. Similarity analysis between training compounds versus active prepared compounds and in silico hits

In an attempt to explain the observed discrepancies between predicted and experimental bioactivities of screening hits and synthesized compounds (e.g., **54**, **56** and **124**) we hypothesized that these differences are because of significant structural differences between training compounds compared to captured hits and synthesized compounds. Accordingly, to test this hypothesis, we employed three library comparison methods (implemented in Discovery Studio 2.5) to assess the structural similarity/diversity between the modeled compounds (**1**–**37**, Table S1 in Supplementary data)³⁴ (library A) compared to captured hits and synthesized compounds (**48**–**111**, **120**–**132**, Table 4, library B), namely, Murcko Assemblies, Bayesian Model and Global Fingerprints. In Murcko Assemblies, the algorithm breaks the ligands of each library into

unique occurrences of molecular rings, ring assemblies, bridge assemblies, chains, Murcko assemblies, or any combination of these. Murcko assemblies are contiguous ring systems plus chains that link two or more rings.⁵⁹ The two libraries are compared using a Tanimoto similarity of the assemblies based on the fragments that are common and unique to each library.⁶⁰ On the other hand, in Bayesian Model approach, two Bayesian models were built, one to learn library A and one to learn library B. Finally, it scores all ligands using both models. A distance is computed as Eq. 2:

$$\text{Distance} = \text{ScoreAA} + \text{ScoreBB} - \text{ScoreAB} - \text{ScoreBA} \quad (2)$$

where ScoreAA is the average score of library A molecules scored by the Bayesian model that learned library A molecules, while ScoreBB is the average score of library B molecules scored by the Bayesian model that learned library B. ScoreAB and ScoreBA are the average scores of libraries A and B molecules scored by the Bayesian models that learned libraries B and A, respectively. The higher the distance, the more dissimilar the libraries are.⁶⁰

Finally, the Global Fingerprint comparison algorithm generates a global fingerprint for all ligands in the training list and all ligands in the hits list and then computes a Tanimoto similarity coefficient between the two libraries.⁶⁰

Table S6 (in Supplementary data) shows the results of the three similarity/diversity assessment procedures. Clearly, the three methods suggest minimal structural similarity between known GP inhibitors and our captured hits, synthesized compounds, which explains the observed differences between predicted and experimental bioactivities.

3. Conclusion

GP inhibitors are currently considered as potential treatments for diabetes. The pharmacophoric space of GP inhibitors was explored via three sets of inhibitors and using CATALYST-HYPOGEN to identify high quality binding model. Subsequently, genetic algorithm and multiple linear regression analysis were employed to access optimal QSAR model capable of explaining anti-GP bioactivity variation across 37 collected GP inhibitors ($r_{30}^2 = 0.69$, $F = 18.70$, $n = 30$, $r_{BS}^2 = 0.69$, $r_{LOO}^2 = 0.58$, r_{PRESS}^2 against 7 external test inhibitors = 0.91). One pharmacophore model emerged in the QSAR equation suggesting the existence of a major binding mode accessible to ligands within GP binding pocket. The QSAR equation and the associated pharmacophoric model were used to guide synthetic exploration of a new series of GP inhibitors that resulted in several novel low micromolar GP inhibitors.

4. Experimental

4.1. Molecular modeling

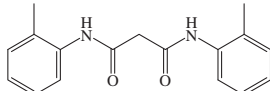
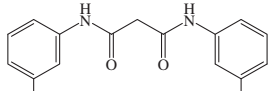
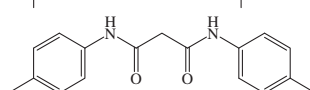
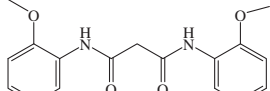
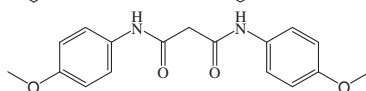
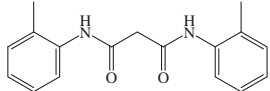
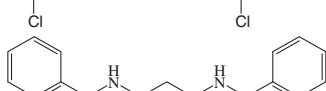
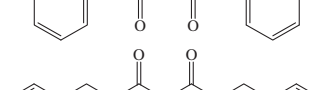
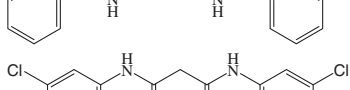
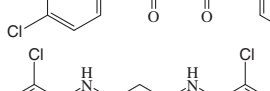
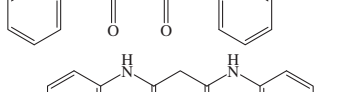
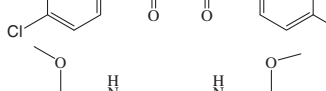
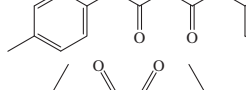
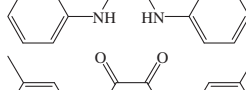
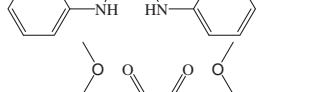
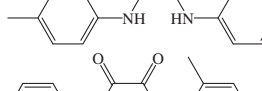
4.1.1. Software and hardware

The following software packages were utilized in the present research.

- CATALYST (Version 4.11), Accelrys Inc. (www.accelrys.com), USA.
- CERIU2 (Version 4.10), Accelrys Inc. (www.accelrys.com), USA.
- CS ChemDraw Ultra (Version 11.0), Cambridge Soft Corp., USA. (<http://www.cambridgesoft.com>), USA.

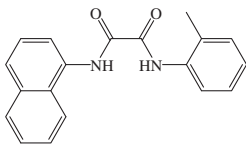
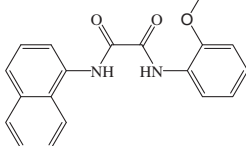
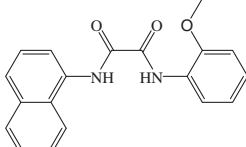
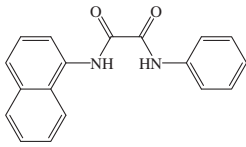
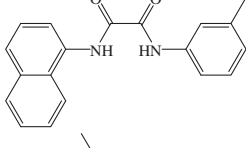
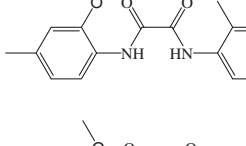
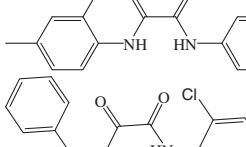
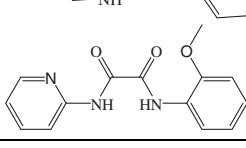
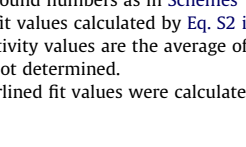
CATALYST and CERIU2 software suites installed on a Silicon Graphics Octane2 desktop workstation equipped with a dual 600 MHz MIPS R14000 processor (1.0 GB RAM) running the Irix 6.5 operating system. Structure drawing was performed employing ChemDraw Ultra 6.0 installed on a Pentium 4 PC.

Table 4
Synthesized compounds with their fit values against (Hypo12/7), corresponding QSAR estimates from Eq. 1 and in vitro anti-GP bioactivities

No. ^a	Structure	Fit value against Hypo12/7 ^b	QSAR Predictions		Experimental		Novelty
			Log (1/IC ₅₀)	IC ₅₀ (μM)	% Inhibition at 10 μM ^c	IC ₅₀ ^c (μM)	
100		1.9	-4.724	52.9	2	ND ^d	Reported ⁷⁰
101		7.7	-3.053	1.2	4	ND ^d	Reported ⁷⁰
102		7.7	-3.273	1.9	3	ND ^d	Reported ⁷⁰
103		5.2	-0.108	1.4	40	ND ^d	Reported ⁷⁰
104		8.7	-4.931	85.3	28	ND ^d	Reported ⁷⁰
105		8.1	-4.387	24.4	25	ND ^d	New
106		5.4	-5.029	106.9	5	ND ^d	Reported ⁷⁰
107		0.5	-6.3	216	1	ND ^d	Reported ⁷¹
108		9.0	-4.731	53.8	24	ND ^d	Reported ⁷²
109		1.8	-5.297	198	23	ND ^d	Reported ⁷⁰
110		9.0	-4.731	53.8	24	ND ^d	Reported ⁷³
111		9.8	-5.532	340	9	ND ^d	New
120		7.9 ^e	-1.988	0.10	55	5.4	Reported ⁷⁴
121		7.4	-2.056	0.11	36	ND ^d	Reported ⁷⁵
122		8.4	-4.474	29.8	24	ND ^d	Reported ⁷⁶
123		6.3	-3.376	7.8	19	ND ^d	New

(continued on next page)

Table 4 (continued)

No. ^a	Structure	Fit value against Hypo12/7 ^b	QSAR Predictions		Experimental		Novelty
			Log (1/IC ₅₀)	IC ₅₀ (μM)	% Inhibition at 10 μM ^c	IC ₅₀ ^c (μM)	
124		<u>7.9</u> ^e	-2.745	0.56	20	ND ^d	New
125		4.04	-3.508	3.22	23	ND ^d	New
126		7.2	-3.902	7.98	15	ND ^d	New
127		6.5	-2.848	0.70	30	ND ^d	Reported ⁷⁷
128		6.7	-2.739	0.55	23	ND ^d	New
129		7.9	-3.748	5.60	24	ND ^d	New
130		9.3	-3.994	9.87	4.0	ND ^d	New
131		<u>8.1</u> ^e	-2.933	0.86	64	3.0	New
132		<u>8.1</u> ^e	-2.545	0.35	5	ND ^d	Reported ⁷⁸

^a Compound numbers as in Schemes 1 and 2.

^b Best-fit values calculated by Eq. S2 in Supplementary data.

^c Bioactivity values are the average of at least duplicate (twice) measurements.

^d ND: not determined.

^e Underlined fit values were calculated by allowing one omitted pharmacophoric feature.

4.1.2. Pharmacophore modelling

The structures of 37 GPa inhibitors (1–37, Table S1 in Supplementary data) were collected from published literature.³⁴ The in vitro bioactivities of the collected inhibitors were expressed as the concentration of the test compound that inhibited the activity of GPa by 50% (IC₅₀). Table S1 in Supplementary data shows the structures and IC₅₀ values of the considered inhibitors. The logarithm of measured IC₅₀ (nM) values were used in pharmacophore modeling and QSAR analysis, thus correlating the data linear to the free energy change. In cases where IC₅₀ is expressed as

being higher than 20,000 nM (e.g., 27, 30, 34 and 35), they were assumed to be 100,000 nM. This assumption is necessary to allow statistical correlation and QSAR analysis. The logarithmic transformation of IC₅₀ values should minimize any potential errors resulting from this assumption.

The two-dimensional (2D) chemical structures of the inhibitors were sketched using ChemDraw Ultra and saved in MDL-mol file format. Subsequently, they were imported into CATALYST, converted into corresponding standard 3D structures and energy minimized to the closest local minimum using the molecular

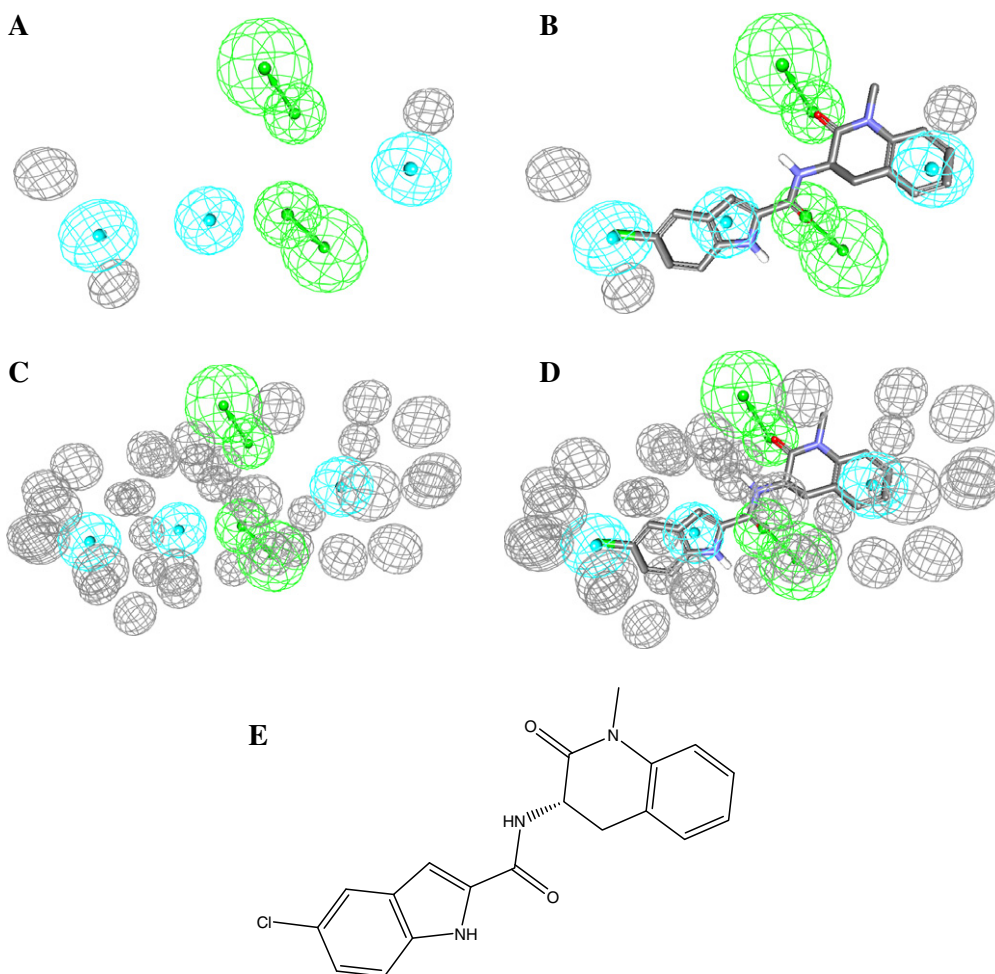


Figure 4. (A) QSAR-selected Hypo12/7, (B) Hypo12/7 mapped against **9** (Table S1 in Supplementary data, $IC_{50} = 25$ nM), (C) sterically-refined Hypo12/7, (D) sterically-refined Hypo12/7 mapped against **9**. Light blue spheres represent Hbic features, green vectored spheres encode for HBAs and grey spheres represent exclusion volumes and (E) chemical structure of **9**.

mechanics CHARMM force field implemented in CATALYST. The resulting 3D structures were utilized as starting conformers for conformational analysis.

The molecular flexibilities of the collected compounds were taken into account by considering each compound as a collection of conformers representing different areas of the conformational space accessible to the molecule within a given energy range. Accordingly, the conformational space of each inhibitor (**1–37**, Table S1 in Supplementary data) was explored adopting the ‘best conformer generation’ option within CATALYST, which is based on the generalized CHARMM force field implemented in the program. Default parameters were employed in the conformation generation procedure, that is, a conformational ensemble was generated with an energy threshold of 20 kcal/mol from the local minimized structure which has the lowest energy level and a maximum limit of 250 conformers per molecule. This search procedure will probably identify the best 3D arrangement of chemical functionalities explaining the activity variations among the training set.³⁷

Subsequently, the collected compounds were used to explore the pharmacophoric space of GPα binding pocket (see detailed experimental procedures under Sections S1 and S2 in Supplementary data).

Afterward, the generated binding hypotheses were clustered as follows: optimal models were clustered into 28 groups (every three models were clustered together) utilizing the hierarchical average linkage method available in CATALYST. Models generated

from each training set were clustered separately, for example, all 84 pharmacophore models generated from training subset **A** were clustered into 28 groups. To select best representative pharmacophores from each cluster, each group members were fitted against the collected compounds (**1–37**, Table S1 in Supplementary data) employing the ‘best’ fit option implemented in CATALYST, and their fit values (calculated from Eq. S4 in Supplementary data) were regressed against the corresponding experimental bioactivities. The highest-ranking models, based on their F-statistic, were selected to represent their corresponding clusters in subsequent QSAR modeling. Table 2 (see Section 2) shows the pharmacophoric features of selected representative binding hypotheses, combined with their CATALYST success criteria.

4.1.3. QSAR modeling

A subset of 30 compounds from the total list of inhibitors (**1–37**, Table S1 in Supplementary data) was utilized as a training set for QSAR modeling. However, since it is essential to access the predictive power of the resulting QSAR models on an external set of inhibitors, the remaining 7 molecules (ca. 20% of the dataset) were employed as an external test subset for validating the QSAR models. The test molecules were selected as follows: The 37 inhibitors (**1–37**, Table S1 in Supplementary data) were ranked according to their IC_{50} values, and then every fifth compound was selected for the test set starting from the high-potency end. This selection considers the fact that the test molecules must represent a range of biological activities similar to that of the training set.

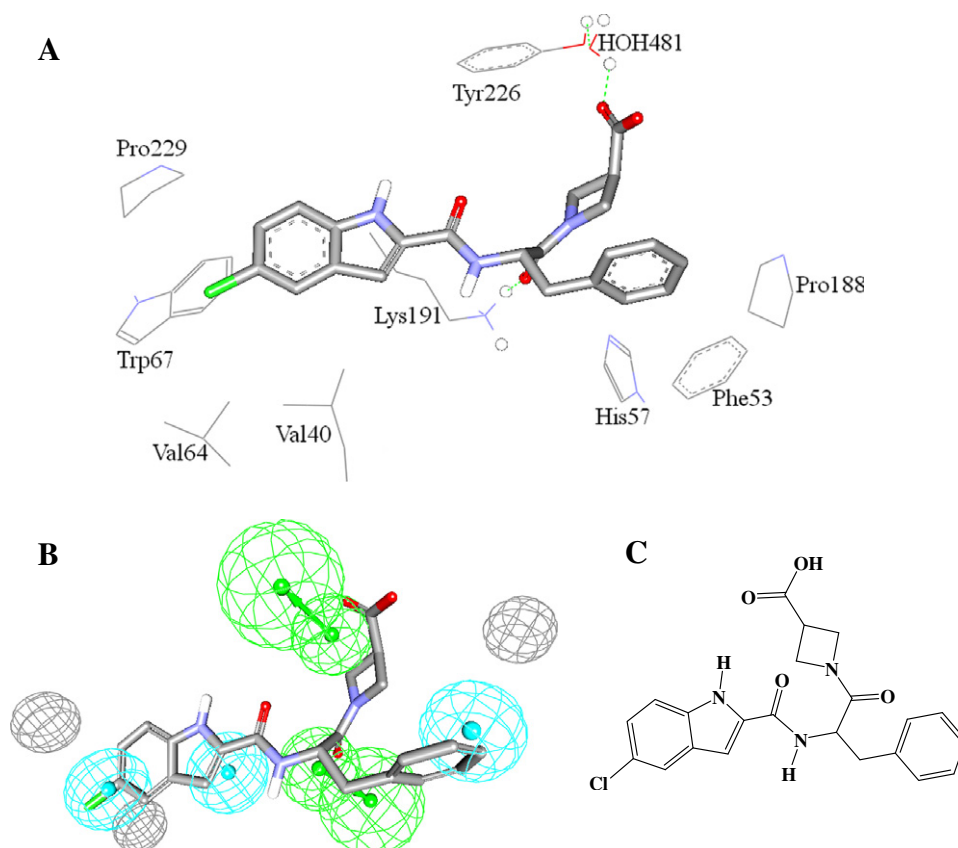


Figure 5. Co-crystallized ligands of GPa X-ray structure 1L5R (resolution = 2.10 Å). (A) Binding pocket of 1L5R complexed with its corresponding co-crystallized ligand (CP-403700), (B) mapping Hypo12/7 against the co-crystallized ligands of 1L5R (rigid mapping) and (C) the chemical structures of the co-crystallized ligand.

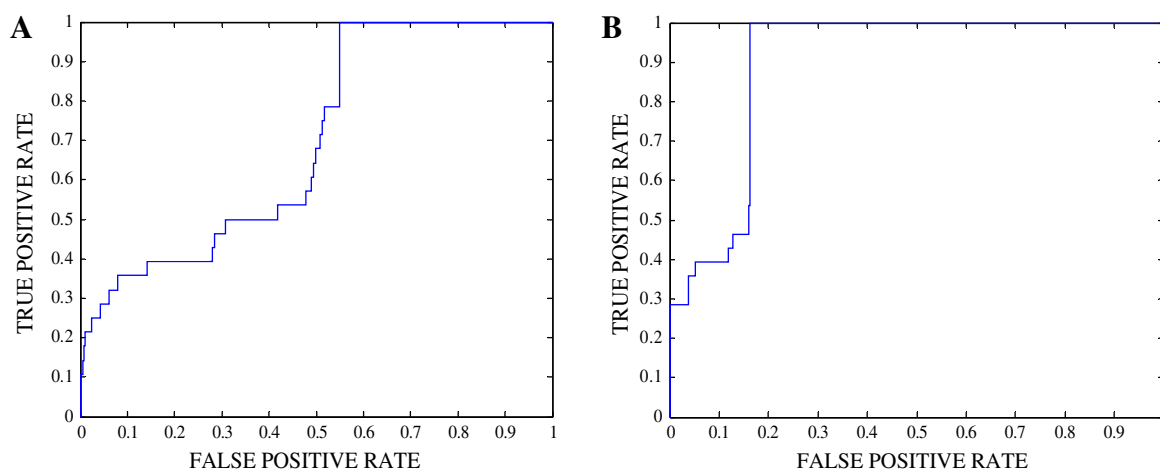
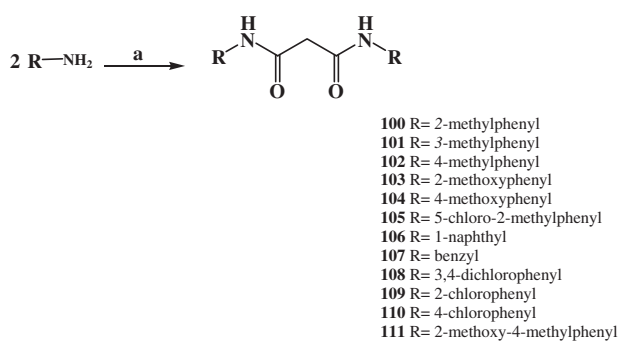


Figure 6. Receiver operating characteristic curves (ROCs) of (A) Hypo12/7 and (B) sterically-refined Hypo12/7.

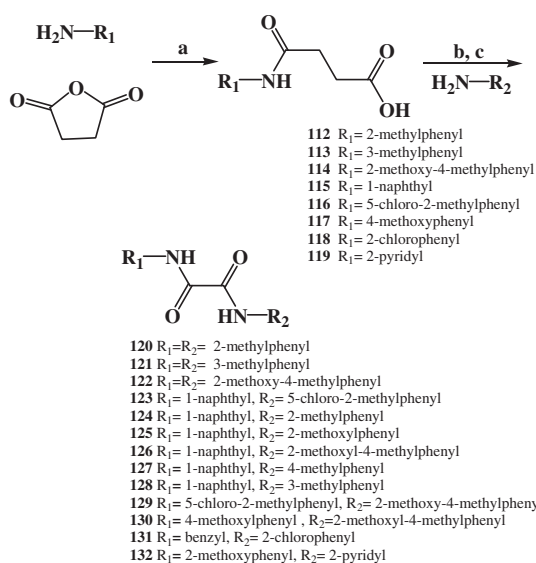
The logarithm of measured $1/IC_{50}$ (nM) values was used in QSAR, thus correlating the data linear to the free energy change. The chemical structures of the inhibitors were imported into CERIU2 as standard 3D single conformer representations in SD format. Subsequently, different descriptor groups were calculated for each compound employing the C2.DESRIPTOR module of CERIU2. The calculated descriptors included various simple and valence connectivity indices, electro-topological state indices and other molecular descriptors (e.g., logarithm of partition coefficient, polarizability, dipole moment, molecular volume, molecular weight,

molecular surface area, etc.).⁴⁴ Furthermore, the training compounds were fitted (using the Best-fit option in CATALYST) against the representative pharmacophores (28 models, Table 2), and their fit values were added as additional descriptors. The fit value for any compound is obtained automatically via Eq. S4 in Supplementary data.³⁷

Genetic function approximation (GFA) was employed to search for the best possible QSAR regression equation capable of correlating the variations in biological activities of the training compounds with variations in the generated descriptors, that is, multiple linear



Scheme 1. Preparation of malonyl diamides **100–111**. Reagents and conditions: (a) Malonyl dichloride in dioxane at 0 °C.



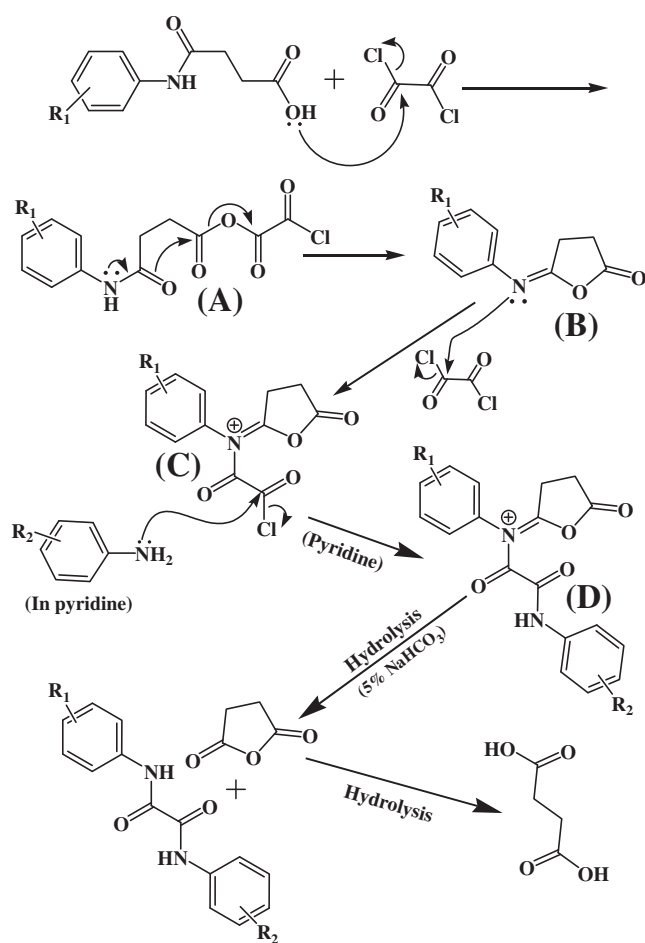
Scheme 2. Preparation of oxalyl diamides. Reagents and conditions: (a) Succinic anhydride in dioxane under reflux conditions, (b) 2 equiv oxalyl chloride (neat) at 0 °C followed by, (c) particular aniline derivative in pyridine.

regression modeling (MLR). GFA techniques rely on the evolutionary operations of ‘crossover and mutation’ to select optimal combinations of descriptors (i.e., chromosomes) capable of explaining bioactivity variation among training compounds from a large pool of possible descriptor combinations, that is, chromosomes population. However, to avoid overwhelming GFA–MLR with large number of poor descriptor populations, the lowest-variance descriptors (20%) were removed prior to QSAR analysis.

Each chromosome is associated with a fitness value that reflects how good it is compared to other solutions. The fitness function employed herein is based on Friedman’s ‘lack-of-fit’ (LOF).⁴⁴

Our preliminary diagnostic trials suggested the following optimal GFA parameters: explore linear, quadratic and spline equations at mating and mutation probabilities of 50%; population size = 500; number of genetic iterations = 30,000 and lack-of-fit (LOF) smoothness parameter = 1.0. However, to determine the optimal number of explanatory terms (QSAR descriptors), it was decided to scan and evaluate all possible QSAR models resulting from 3 to 6 explanatory terms.

All QSAR models were validated employing leave one-out cross-validation (r_{LOO}^2), bootstrapping (r_{BS}^2) and predictive r^2 (r_{PRESS}^2) calculated from the test subsets. The predictive r_{PRESS}^2 is defined as:



Scheme 3. Proposed mechanism of *N,N*-di-oxalamide derivatives synthesis.

$$r_{PRESS}^2 = SD-PRESS/SD \quad (3)$$

where SD is the sum of the squared deviations between the biological activities of the test set and the mean activity of the training set molecules, PRESS is the squared deviations between predicted and actual activity values for every molecule in the test set.

4.1.4. Receiver operating characteristic (ROC) curve analysis

Successful pharmacophore models (Hypo12/7 and refined pharmacophore) were further validated by assessing their abilities to selectively capture diverse GP active compounds from a large list of decoys employing ROC analysis.

Therefore, it was necessary to prepare valid evaluation structural database (testing set) that contains an appropriate list of decoy compounds in combination with diverse list of known active compounds. The decoy list was prepared as described by Verdonk and co-workers.^{62,63} Briefly, the decoy compounds were selected based on three basic one-dimensional (1D) properties that allow the assessment of distance (*D*) between two molecules (e.g., *i* and *j*): (1) the number of hydrogen-bond donors (NumHBD); (2) number of hydrogen-bond acceptors (NumHBA) and (3) count of nonpolar atoms (NP, defined as the summation of Cl, F, Br, I, S and C atoms in a particular molecule). For each active compound in the testing set, the distance to the nearest other active compound is assessed using their euclidean distance (Eq. 4):

$$D(i, j) = \sqrt{(\text{NumHBD}_i - \text{NumHBD}_j)^2 + (\text{NumHBA}_i - \text{NumHBA}_j)^2 + (\text{NP}_i - \text{NP}_j)^2} \quad (4)$$

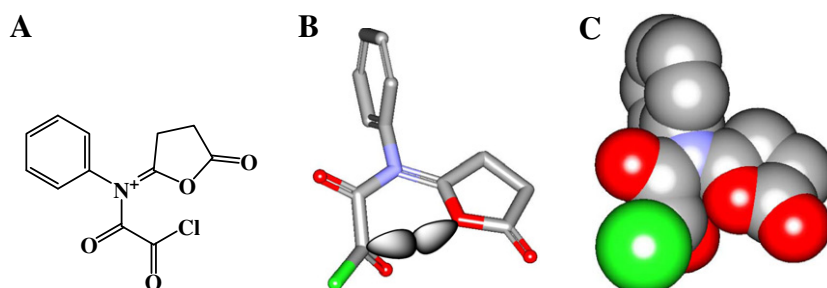


Figure 7. (A) The chemical structure of the proposed isoimidium-oxalylchloride adduct, (B) energy-minimized structure of the adduct showing an overlap between the oxygen unshared pair of electrons and the lowest unoccupied molecular orbital (LUMO) of the acyl chloride and (C) CPK presentation of the adduct showing the close proximity of the isoimidium oxygen and the carbon of the acyl chloride fragment.

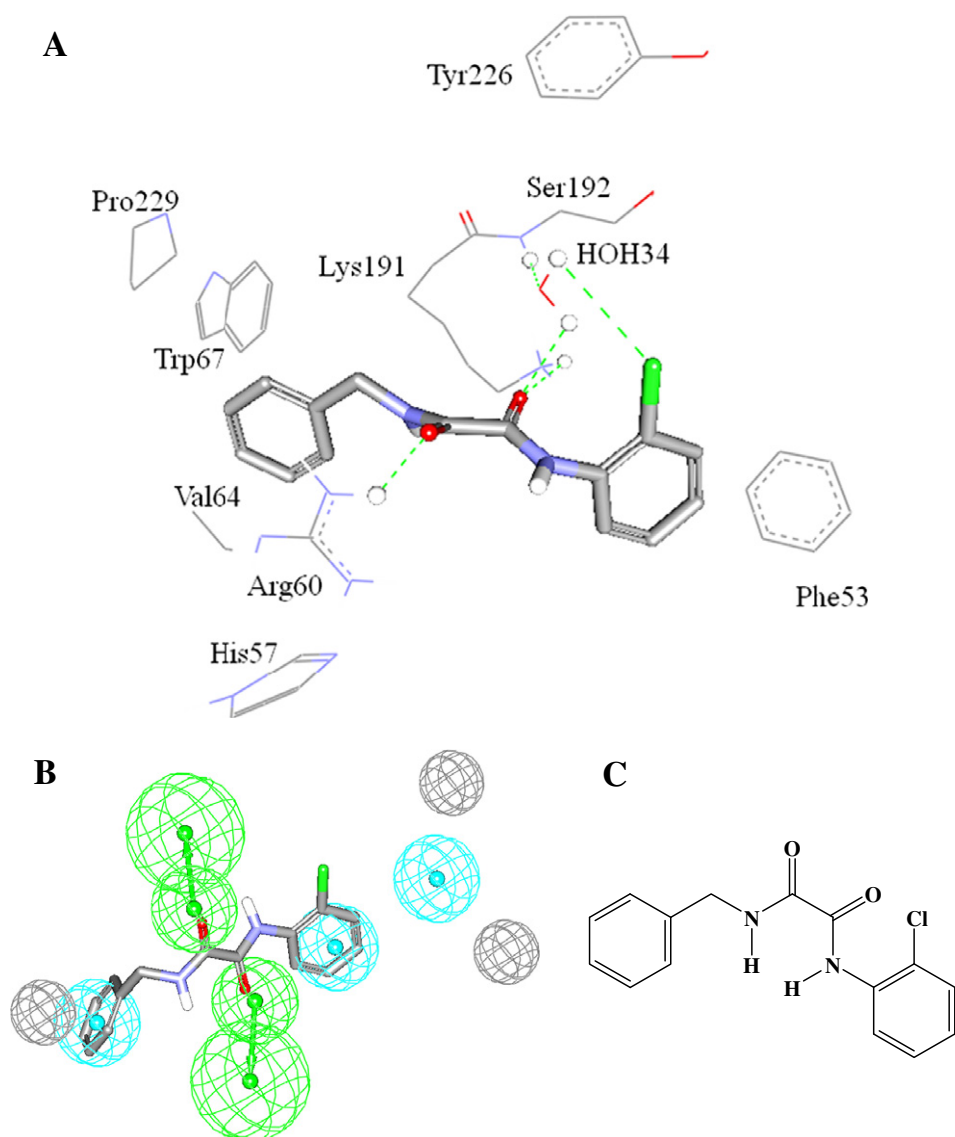


Figure 8. Prepared compound **131** ($IC_{50} = 3 \mu M$, Table 4). (A) Compound **131** docked into the binding pocket of GPa (PDB code: 1L5R, resolution 2.10 Å), (B) **131** fitted against Hypo12/7 and (C) chemical structure of **131**.

The minimum distances are then averaged over all active compounds (D_{min}). Subsequently, for each active compound in the testing set, 33 decoys were randomly chosen from the ZINC database.⁶⁴ The decoys were selected in such a way that they did not exceed D_{min} distance from their corresponding active compound.

Moreover, to further diversify the actives members, that is, to avoid close similarity among actives in the testing set, any active compound having zero distance ($D(i, j)$) from other active compound(s) in the testing set were excluded. Active testing compounds were defined as those possessing GP inhibition ranging

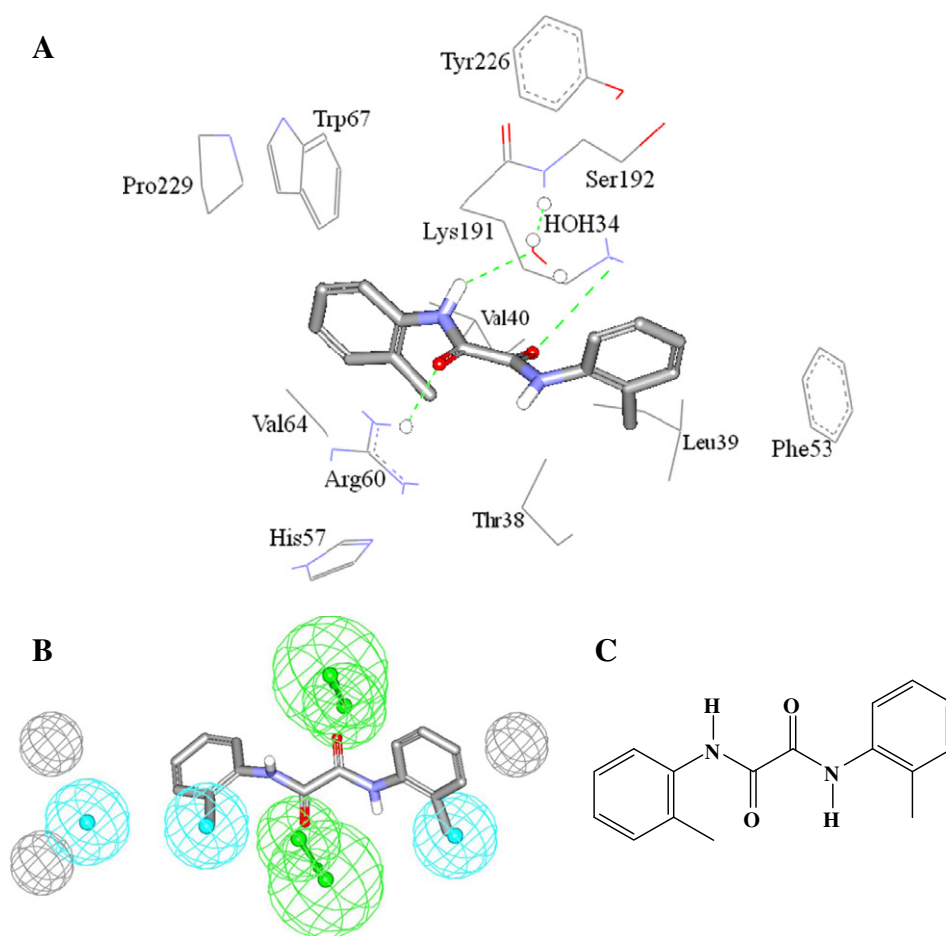


Figure 9. Synthesized compound **120** ($IC_{50} = 5 \mu\text{M}$, Table 3). (A) Compound **120** docked into the binding pocket of GPa (PDB code: 1L5R, resolution 2.10 Å), (B) **120** fitted against Hypo12/7 and (C) chemical structure of **120**.

from 25 to 6400 nM. The testing set included 28 active compounds and 909 ZINC compounds.

The testing set (937 compounds) was screened by each particular pharmacophore (for ROC analysis) employing the 'Best flexible search' option implemented in CATALYST, while the conformational spaces of the compounds were generated employing the 'Fast conformation generation option' implemented in CATALYST. Compounds missing one or more features were discarded from the hit list. The in silico hits were scored employing their fit values as calculated by Eq. S4 in Supplementary data.

The ROC curve analysis describes the sensitivity (Se or true positive rate, Eq. 5) for any possible change in the number of selected compounds (n) as a function of $(1-\text{Sp})$. Sp is defined as specificity or true negative rate (Eq. 6).^{62,65}

$$\text{Se} = \frac{\text{Number of selected actives}}{\text{Total number of actives}} = \frac{\text{TP}}{\text{TP} + \text{FN}} \quad (5)$$

$$\text{Sp} = \frac{\text{Number of discarded inactives}}{\text{Total number of inactives}} = \frac{\text{TN}}{\text{TN} + \text{FP}} \quad (6)$$

where TP is the number of active compounds captured by the virtual screening method (true positives), FN is the number of active compounds discarded by the virtual screening method, TN is the number of discarded decoys (presumably inactives), while FP is the number of captured decoys (presumably inactives).

If all molecules scored by a virtual screening (VS) protocol with sufficient discriminatory power are ranked according to their score (i.e., fit values), starting with the best-scored molecule and ending

with the molecule that got the lowest score, most of the actives will have a higher score than the decoys. Since some of the actives will be scored lower than decoys, an overlap between the distribution of active molecules and decoys will occur, which will lead to the prediction of false positives and false negatives.^{62,65} The selection of one score value as a threshold strongly influences the ratio of actives to decoys and therefore, the validation of a VS method. The ROC curve method avoids the selection of a threshold by considering all Se and Sp pairs for each score threshold.⁶⁸ A ROC curve is plotted by setting the score of the active molecule as the first threshold. Afterwards, the number of decoys within this cutoff is counted and the corresponding Se and Sp pair is calculated. This calculation is repeated for the active molecule with the second highest score and so forth, until the scores of all actives are considered as selection thresholds.

The ROC curve representing ideal distributions, where no overlap between the scores of active molecules and decoys exists, proceeds from the origin to the upper-left corner until all the actives are retrieved and Se reaches the value of 1. Thereafter, only decoys can be found using the VS method. Thus, the ideal ROC curve continues as a horizontal straight line to the upper-right corner where all actives and all decoys are retrieved, which corresponds to $\text{Se} = 1$ and $\text{Sp} = 0$. In contrast to that, the ROC curve for a set of actives and decoys with randomly distributed scores tends towards the $\text{Se} = 1 - \text{Sp}$ line asymptotically with increasing number of actives and decoys.⁶⁵ The success of a particular virtual screening workflow can be judged from the following criteria:

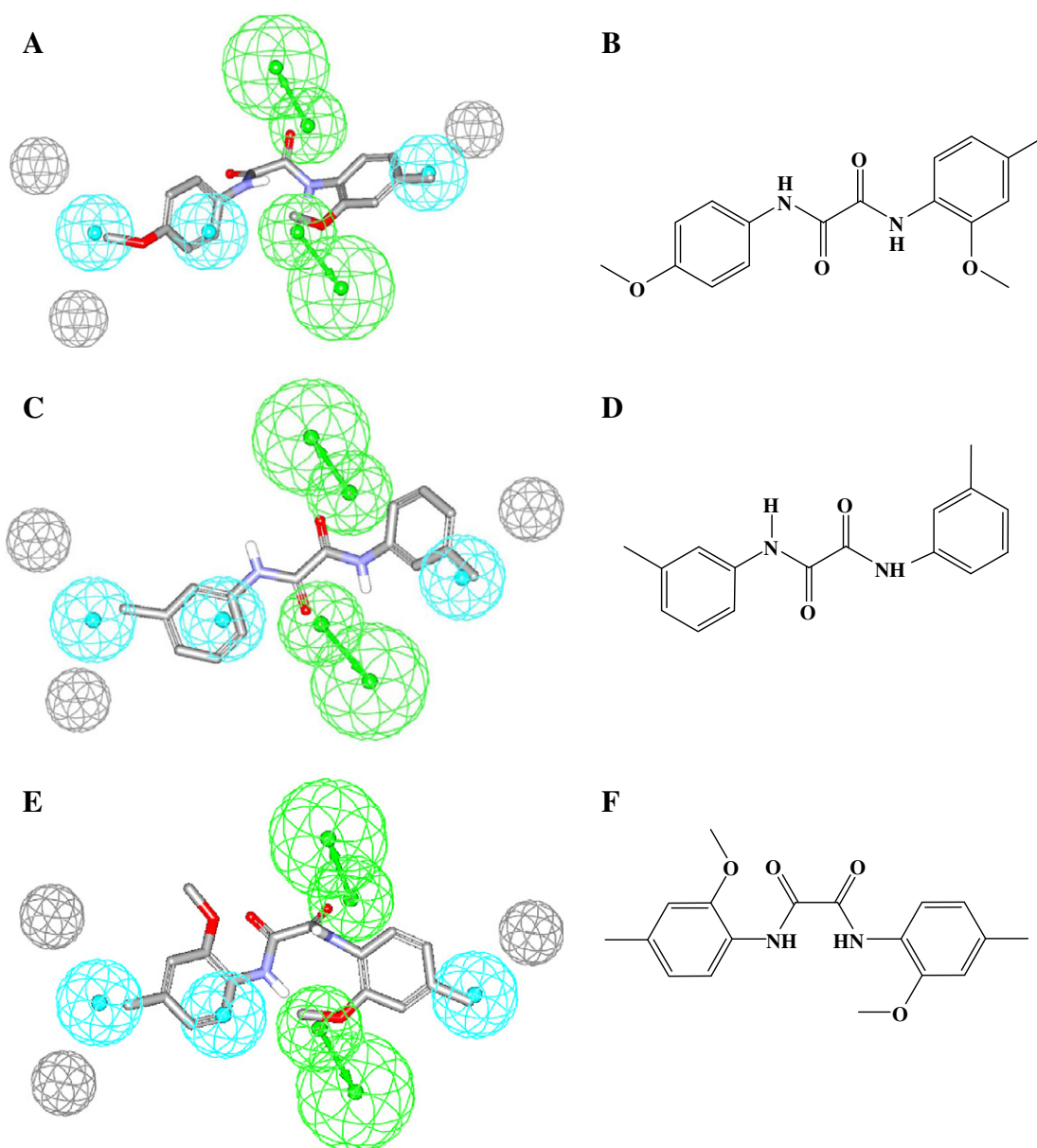


Figure 10. (A) Compound **130** mapped against Hypo12/7, (B) chemical structure of **130**, (C) **121** mapped against Hypo12/7, (D) chemical structure of **121**, (E) **122** mapped against Hypo12/7 and (F) chemical structure of **122**.

- (1) Area under the ROC curve (AUC).⁶⁵ In an optimal ROC curve an AUC value of 1 is obtained; however, random distributions cause an AUC value of 0.5. Virtual screening that performs better than a random discrimination of actives and decoys retrieve an AUC value between 0.5 and 1, whereas an AUC value lower than 0.5 represents the unfavorable case of a virtual screening method that has a higher probability to assign the best scores to decoys than to actives.^{62,65}
- (2) Overall accuracy (ACC): describes the percentage of correctly classified molecules by the screening protocol (equation 7). Testing compounds are assigned a binary score value of zero (compound not captured) or one (compound captured).^{62,66,67}

$$\text{ACC} = \frac{\text{TP} + \text{TN}}{N} = \frac{A}{N} \cdot \text{Se} + \left(1 - \frac{A}{N}\right) \cdot \text{Sp} \quad (7)$$

where N is the total number of compounds in the testing database, A is the number of true actives in the testing database.
- (3) Overall specificity (SPC): describes the percentage of discarded inactives by the particular virtual screening workflow. Inactive test compounds are assigned a binary score value of zero (compound not captured) or one (compound captured) regardless to their individual fit values.^{62,66,67}
- (4) Overall true positive rate (TPR or overall sensitivity): describes the fraction percentage of captured actives from the total number of actives. Active test compounds are assigned a binary score value of zero (compound not captured) or one (compound captured) regardless to their individual fit values.
- (5) Overall false negative rate (FNR or overall percentage of discarded actives): describes the fraction percentage of active compounds discarded by the virtual screening method. Discarded active test compounds are assigned a binary score value of zero (compound not captured) or one (compound captured) regardless to their individual fit values.

4.1.5. In silico screening for new GP inhibitors

Refined Hypo12/7 was employed as 3D search queries against the NCI using the 'Best Flexible Database Search' option implemented within CATALYST. NCI hits were filtered based on Lipinski's and Veber's rules.^{47,48} The remaining hits were fitted against Hypo12/7 using the 'best-fit' approach implemented within CATALYST. Subsequently, the fit values together with other relevant molecular descriptors were substituted in QSAR Eq. 1 to predict anti-GP IC₅₀ values. The highest-ranking hits were subsequently tested in vitro.

4.2. Synthetic procedures

Melting points were measured using Gallenkamp melting point apparatus and are uncorrected. ¹H NMR and ¹³C NMR spectra were collected on a Bruker NMR400 spectrometer. High resolution mass spectrometry was performed using LC Mass Bruker Apex-IV mass spectrometer utilizing an electrospray interface. Infrared spectra were recorded using WQF-520 FTIR spectrometer. The samples were analyzed as KBr pellets. Analytical thin layer chromatography (TLC) was carried out using pre-coated alumina plates and visualized by UV light (at 254 and/or 360 nm) using different combinations of mobile phase to ensure purity. Elemental analysis was performed using EuroVector elemental analyzer. Chemicals and solvents were used without further purification.

4.2.1. Preparation of malonyl diamide derivatives (100–111)

Malonyl diamide derivatives were prepared as described earlier.⁴⁹ Briefly: To a magnetically stirred ice bath-cooled solution of the selected amine (14 mmol), and triethylamine (14 mmol, 1.4 g) in dioxane (20 ml), malonyl dichloride (1.0 g, 7.0 mmol) solution in dioxane (20 ml) was added dropwise over 15 min. The reaction mixture was stirred at 0 °C for one hour. Subsequently, HCl (2 N, 50 ml) was added to the reaction suspension and stirred for 30 minutes. Finally, the mixture was filtered to afford the products as whitish to gray solids that were further washed by stirring in water (50 mL) for 30 min (Scheme 1).

Using the same general procedure, the following compounds were prepared.

4.2.1.1. N¹,N³-Di-*o*-tolylmalonamide (100). Yield (1.4 g, 56%): mp: 192–194 °C (cryst. water); ν_{\max} (KBr): 3273, 1687 cm⁻¹; ¹H NMR (400 MHz, DMSO-*d*₆): δ 2.20 (s, 6H, CH₃), 3.42 (s, 2H, CH₂, D-exchange), 7.08 (m, 2H), 7.20 (m, 4H), 7.52 (m, 2H), 9.67 ppm (br s, 2H, NH) ppm; ¹³C NMR (100 MHz, DMSO-*d*₆): δ 20.40 (2 × CH₃), 46.56 (CH₂), 126.94 (2 × CH), 127.81 (2 × CH), 128.68 (2 × CH), 132.98 (2 × CH), 133.72 (2 × C), 138.59 (2 × C), 168.38 (2 × C=O) ppm; HRMS-ESI *m/z* [M+Na]⁺ calcd for C₁₇H₁₈N₂NaO₂: 305.12659, found 305.12605. Anal. Calcd for C₁₇H₁₈N₂O₂: C, 72.32; H, 6.43; N, 9.92. Found: C, 69.99; H, 6.73; N, 9.23.

4.2.1.2. N¹,N³-Di-*m*-tolylmalonamide (101). Yield (1.4 g, 56%): mp: 150–153 °C (cryst. water); ν_{\max} (KBr): 3273, 1687 cm⁻¹; ¹H NMR (400 MHz, DMSO-*d*₆): δ 2.27 (s, 6H, CH₃), 3.45 (2H, CH₂, D-exchange), 6.86 (m, 2H), 7.18 (m, 2H), 7.37 (m, 2H), 7.43 (m, 2H), 10.10 ppm (br s, 2H, NH) ppm; ¹³C NMR (100 MHz, DMSO-*d*₆): δ 23.83 (2 × CH₃), 48.45 (CH₂), 118.86 (2 × CH), 122.19 (2 × CH), 126.78 (2 × CH), 131.27 (2 × CH), 140.62 (2 × C), 141.39 (2 × C), 167.95 (2 × C=O) ppm; HRMS-ESI *m/z* [M+Na]⁺ calcd for C₁₇H₁₈N₂NaO₂: 305.12659, found 305.12605. Anal. Calcd for C₁₇H₁₈N₂O₂: C, 72.32; H, 6.43. Found: C, 70.19; H, 6.35.

4.2.1.3. N¹,N³-Di-*p*-tolylmalonamide (102). Yield (1.5 g, 60%): mp: 242–245 °C (cryst. water); ν_{\max} (KBr): 3273, 1674, 1651 cm⁻¹; ¹H NMR (400 MHz, DMSO-*d*₆): δ 2.23 (s, 6H, CH₃), 3.41

(2H, CH₂, D-exchange), 7.09 (d, *J* = 8 Hz, 4H), 7.47 (d *J* 8, 4H), 10.10 ppm (br s, 2H, NH) ppm; ¹³C NMR (100 MHz, DMSO-*d*₆): δ 23.07 (2 × CH₃), 48.34 (CH₂), 121.68 (4 × CH), 131.80 (4 × CH), 135.02 (2 × C), 138.96 (2 × C), 167.82 (2 × C=O) ppm; HRMS-ESI *m/z* [M+Na]⁺ calcd for C₁₇H₁₈N₂NaO₂: 305.12659, found 305.12605. Anal. Calcd for C₁₇H₁₈N₂O₂: C, 72.32; H, 6.43. Found: C, 69.38; H, 6.28.

4.2.1.4. N¹,N³-Bis-(2-methoxy-phenyl)-malonamide (103). Yield (1.5 g, 60%): mp: 160–163 °C (cryst. water); ν_{\max} (KBr): 3367, 3292, 1676 cm⁻¹; ¹H NMR (400 MHz, DMSO-*d*₆): δ 3.44 (2H, CH₂, D-exchange), 3.70 (s, 6H, OCH₃), 6.93 (m, 2H), 7.05 (m, 4H), 8.02 (m, 2H), 9.70 ppm (br s, 2H, NH) ppm; ¹³C NMR (100 MHz, DMSO-*d*₆): δ 47.0 (CH₂), 58.37 (2 × OCH₃), 113.78 (2 × CH), 122.96 (2 × CH), 124.01 (2 × CH), 127.18 (2 × CH), 129.57 (2 × C), 151.89 (2 × C), 168.50 (2 × C=O) ppm; HRMS-ESI *m/z* [M+Na]⁺ calcd for C₁₇H₁₈N₂NaO₄: 337.11642, found 337.11588. Anal. Calcd for C₁₇H₁₈N₂O₄: C, 64.96; H, 5.77. Found: C, 62.41; H, 5.55.

4.2.1.5. N¹,N³-Bis-(4-methoxy-phenyl)-malonamide (104). Yield (2 g, 74%): mp: 180–184 °C (cryst. water); ν_{\max} (KBr): 3280, 1682 cm⁻¹; ¹H NMR (400 MHz, DMSO-*d*₆): δ 3.41 (2H, CH₂, D-exchange), 3.70 (s, 6H, OCH₃), 6.87 (d, *J* = 8 Hz, 4H), 7.50 (d, *J* = 8 Hz, 4H), 10.03 ppm (br s, 2H, NH) ppm; ¹³C NMR (100 MHz, DMSO-*d*₆): δ 48.20 (CH₂), 57.79 (2 × OCH₃), 116.52 (4 × CH), 123.19 (4 × CH), 134.68 (2 × C), 157.93 (2 × C), 167.57 (2 × C=O) ppm; HRMS-ESI *m/z* [M+Na]⁺ calcd for C₁₇H₁₈N₂NaO₄: 337.11642, found 337.11588. Anal. Calcd for C₁₇H₁₈N₂O₄: C, 64.96; H, 5.77. Found: C, 63.02; H, 5.77.

4.2.1.6. N¹,N³-Bis-(5-chloro-2-methylphenyl)-malonamide (105). Yield (1.8 g, 60%): mp: 157–158 °C (cryst. water); ν_{\max} (KBr): 3280, 1655 cm⁻¹; ¹H NMR (400 MHz, DMSO-*d*₆): δ 2.20 (s, 6H, CH₃), 3.55 (2H, CH₂, D-exchange), 7.11 (m, 2H), 7.22 (m, 2H), 7.68 (m, 2H), 9.76 ppm (br s, 2H, NH) ppm; ¹³C NMR (100 MHz, DMSO-*d*₆): δ 19.87 (2 × CH₃), 46.60 (CH₂), 125.97 (2 × CH), 127.26 (2 × CH), 132.06 (2 × C), 132.62 (2 × C), 134.45 (2 × CH), 139.84 (2 × C), 168.64 (2 × C=O) ppm; HRMS-ESI *m/z* [M+Na]⁺ calcd for C₁₇H₁₆N₂Cl₂NaO₂: 373.04865, found 373.04810. Anal. Calcd for C₁₇H₁₆Cl₂N₂O₂: C, 58.13; H, 4.59; N, 7.98. Found: C, 57.98; H, 4.47; N, 7.87.

4.2.1.7. N¹-(Naphthalen-1-yl)-N³-(naphthalen-1-yl)malonamide (106). Yield (1.8 g, 60%): mp: 220–223 °C (cryst. water); ν_{\max} (KBr): 3300, 1640 cm⁻¹; ¹H NMR (400 MHz, DMSO-*d*₆): δ 3.55 (2H, CH₂, D-exchange), 7.55 (m, 6H), 7.80 (m, 4H), 7.94 (m, 2H), 8.18 (m, 2H), 10.36 ppm (br s, 2H, NH) ppm; ¹³C NMR (100 MHz, DMSO-*d*₆): δ 47.10 (CH₂), 124.11 (2 × CH), 125.26 (2 × CH), 128.13 (2 × CH), 128.28 (2 × CH), 128.71 (2 × CH), 130.22 (2 × CH), 130.84 (2 × CH), 135.82 (2 × C), 135.95 (2 × C), 136.38 (2 × C), 169.25 (2 × C=O) ppm; HRMS-ESI *m/z* [M+Na]⁺ calcd for C₂₃H₁₈N₂NaO₂: 377.12659, found 377.12605. Anal. Calcd for C₂₃H₁₈N₂O₂: C, 77.95; H, 5.12; N, 7.90. Found: C, 76.70; H, 4.76; N, 7.73.

4.2.1.8. N¹,N³-Dibenzyl-malonamide (107). Yield (1.4 g, 56%): mp: 139–142 °C (cryst. water); ν_{\max} (KBr): 3284, 1655 cm⁻¹; ¹H NMR (400 MHz, DMSO-*d*₆): δ 3.42 (2H, CH₂, D-exchange), 4.24 (m, 4H, CH₂), 7.28 (m, 10H), 8.51 ppm (br s, 2H, NH) ppm; ¹³C NMR (100 MHz, DMSO-*d*₆): δ 44.87 (CH₂), 46.12 (2 × CH₂), 129.43 (2 × CH), 129.86 (4 × CH), 131.15 (4 × CH), 141.84 (2 × C), 169.52 (2 × C=O) ppm; HRMS-ESI *m/z* [M+Na]⁺ calcd for C₁₇H₁₈N₂NaO₂: 305.12659, found 305.12605. Anal. Calcd for C₁₇H₁₈N₂O₂: C, 72.32; H, 6.43. Found: C, 69.35; H, 5.62.

4.2.1.9. *N*¹,*N*³-Bis(3,4-dichlorophenyl)malonamide (108). Yield (1.7 g, 61%): mp: 214–216 °C (cryst. water); ν_{\max} (KBr): 3276, 1655 cm^{-1} ; ^1H NMR (400 MHz, DMSO-*d*₆): δ 3.51 (2H, CH₂, D-exchange), 7.47 (m, 2H), 7.54 (m, 2H), 7.98 (m, 2H), 10.50 ppm (br s, 2H, NH) ppm; ^{13}C NMR (100 MHz, DMSO-*d*₆): δ 48.62 (CH₂), 121.78 (2 × CH), 122.86 (2 × CH), 127.59 (2 × C), 133.37 (2 × CH), 133.71 (2 × C), 141.48 (2 × C) 168.20 (2 × C=O) ppm; HRMS-ESI *m/z* [*M*+Na]⁺ calcd for C₁₅H₁₀Cl₄N₂NaO₂: 412.93940, found 412.93886. Anal. Calcd for C₁₅H₁₀Cl₄N₂O₂: C, 45.95; H, 2.57. Found: C, 45.23; H, 2.82.

4.2.1.10. *N*¹,*N*³-Bis(2-chlorophenyl)malonamide (109). Yield (1.8 g, 14 mmol) and triethylamine (1.4 g, 14 mmol) to yield the title compound as white powder (1.5 g, 53%): mp: 168–170 °C (cryst. water); ν_{\max} (KBr): 3276, 1655 cm^{-1} ; ^1H NMR (400 MHz, DMSO-*d*₆): δ 3.57 (2H, CH₂, D-exchange), 7.19 (m, 2H), 7.34 (m, 2H), 7.49 (m, 2H), 7.88 (m, 2H), 10.10 ppm (br s, 2H, NH) ppm; ^{13}C NMR (100 MHz, DMSO-*d*₆): 46.5 (CH₂), 127.61 (2 × CH), 128.05 (2 × CH), 128.88 (2 × CH), 130.23 (2 × CH), 132.15 (2 × C), 137.05 (2 × C) 168.61 (2 × C=O) ppm; HRMS-ESI *m/z* [*M*+Na]⁺ calcd for C₁₅H₁₂Cl₂N₂NaO₂: 345.01735, found 345.01680. Anal. Calcd for C₁₅H₁₂Cl₂N₂O₂: C, 55.75; H, 3.74. Found: C, 54.55; H, 3.83.

4.2.1.11. *N*¹,*N*³-Bis(4-chlorophenyl)malonamide (110). Yield (2 g, 61%): mp: 255–258 °C (cryst. water); ν_{\max} (KBr): 3276, 1655 cm^{-1} ; ^1H NMR (400 MHz, DMSO-*d*₆): δ 3.52 (2H, CH₂, D-exchange), 7.34 (d, *J* = 8 Hz, 4H), 7.62 (d, *J* = 8 Hz, 4H), 10.33 ppm (br s, 2H, NH) ppm; ^{13}C NMR (100 MHz, DMSO-*d*₆): δ 48.54 (CH₂), 123.22 (4 × CH), 123.31 (2 × C), 129.69 (4 × CH), 140.42 (2 × C), 168.06 (2 × C=O) ppm; HRMS-ESI *m/z* [*M*+Na]⁺ calcd for C₁₅H₁₂Cl₂N₂NaO₂: 345.01735, found 345.01680. Anal. Calcd for C₁₅H₁₂Cl₂N₂O₂: C, 55.75; H, 3.74; N, 8.67. Found: C, 57.57; H, 3.93; N, 8.65.

4.2.1.12. *N*¹,*N*³-Bis(2-methoxy-4-methylphenyl) malonamide (111). Yield (1.7 g, 58%): mp: 160–163 °C (cryst. water); ν_{\max} (KBr): 3280, 1640 cm^{-1} ; ^1H NMR (400 MHz, DMSO-*d*₆): δ 2.20 (s, 6H, CH₃), 3.45 (2H, CH₂, D-exchange), 3.67 (s, 6H, OCH₃), 6.88 (m, 4H), 7.85 (m, 2H), 9.61 ppm (br s, 2H, NH) ppm; ^{13}C NMR (100 MHz, DMSO-*d*₆): δ 23.14 (2 × CH₃), 47.09 (CH₂), 58.43 (2 × OCH₃), 113.65 (2 × CH), 124.76 (2 × CH), 127.33 (2 × CH), 129.24 (2 × C), 131.68 (2 × C), 149.88 (2 × C), 168.40 (2 × C=O) ppm; HRMS-ESI *m/z* [*M*+Na]⁺ calcd for C₁₉H₂₂N₂NaO₄: 365.14772, found 365.14718. Anal. Calcd for C₁₉H₂₂N₂O₄: C, 66.65; H, 6.48. Found: C, 63.88; H, 6.28

4.2.2. Preparation of succinic monoamide derivatives

To a magnetically stirred solution of the selected aromatic amine (0.01 mol) in anhydrous dioxane (30 ml), succinic anhydride (0.01 mol) was added and the resulting suspension was refluxed for 24 h. Subsequently, the reaction mixture was cooled to room temperature. Subsequently, petroleum ether (200 mL) was added to the reaction mixture to yield the succinic monoamide derivatives (112–119, see Scheme 2) as white to grey solids. Using the same general procedure, the following compounds were synthesized.

4.2.2.1. *N*-*o*-Tolyl-succinamic acid (112). Yield (1.07 g, 0.01 mmol) to yield the title compound as white powder (1.4 g, 70%): mp: 144–146 °C (cryst. diethylether); ν_{\max} (KBr): 3300–2700, 1655 cm^{-1} . ^1H NMR (400 MHz, DMSO-*d*₆): δ 1.78 (s, 3H, CH₃), 2.62 (m, 2H, CH₂), 2.76 (m, 2H, CH₂), 7.48 (m, 3H), 8.00 (m, 1H), 10.27 (br s, 1H, NH), 12.13 (br s, 1H, OH) ppm; ^{13}C NMR (100 MHz, DMSO-*d*₆): δ 23.82 (CH₃), 31.24 (CH₂), 33.71 (CH₂), 118.77 (CH), 122.10 (CH), 126.27 (CH), 131.13 (CH), 133.61 (C), 140.92 (C), 172.62 (C=O), 176.52 (C=O) ppm. HRMS-ESI *m/z* [*M*-H]⁺ calcd for C₁₁H₁₂NO₃: 206.08172, found 206.08227.

4.2.2.2. *N*-*m*-Tolyl-succinamic acid (113). Yield (1.4 g, 70%): mp: 136–140 °C (cryst. diethylether); ν_{\max} (KBr): 3300–2700, 1693 cm^{-1} . ^1H NMR (400 MHz, DMSO-*d*₆): δ 1.80 (s, 3H, CH₃), 2.58 (m, 2H, CH₂), 2.73 (m, 2H, CH₂), 7.51 (m, 3H), 8.00 (m, 1H), 10.21 (br s, 1H, NH), 12.00 (br s, 1H, OH) ppm; ^{13}C NMR (100 MHz, DMSO-*d*₆): δ 23.72 (CH₃), 31.21 (CH₂), 33.66 (CH₂), 116.71 (CH), 121.90 (CH), 125.27 (CH), 131.43 (CH), 134.51 (C), 140.89 (C), 172.52 (C=O), 176.31 (C=O) ppm; HRMS-ESI *m/z* [*M*-H]⁺ calcd for C₁₁H₁₂NO₃: 206.08172, found 206.08227.

4.2.2.3. *N*-4-Methyl-*o*-anisidine-succinamic acid (114). Yield (1.4 g, 70%): mp: 147–150 °C (cryst. diethylether); ν_{\max} (KBr): 3300–2650, 1701 cm^{-1} . ^1H NMR (400 MHz, DMSO-*d*₆): δ 2.01 (s, 3H, CH₃), 2.35 (m, 2H, CH₂), 2.72 (m, 2H, CH₂), 3.98 (s, 3H, OCH₃), 7.03 (m, 1H), 7.18 (m, 1H), 7.71 (m, 1H), 9.83 (br s, 1H, NH), 12.14 ppm (br s, 1H, OH) ppm; ^{13}C NMR (100 MHz, DMSO-*d*₆): δ 23.51 (CH₃), 31.01 (CH₂), 33.521 (CH₂), 57.97 (OCH₃), 116.42 (CH), 123.08 (CH), 127.94 (CH), 135.15 (C), 157.62 (C), 161.44 (C), 172.17 (C=O), 176.53 (C=O) ppm; HRMS-ESI *m/z* [*M*-H]⁺ calcd for C₁₂H₁₄NO₄: 236.9228, found 236.09283.

4.2.2.4. *N*-Naphthylamine-succinamic acid (115). Yield (1.43 g, 0.01 mmol) to yield the title compound as faint violet powder (1.4 g, 70%): mp: 147–150 °C (cryst. diethylether); ν_{\max} (KBr): 3300–2600, 1714 cm^{-1} . ^1H NMR (300 MHz, DMSO-*d*₆): δ 2.55 (t, 2H, CH₂), 2.70 (t, 2H, CH₂), 7.38 (m, 4H), 7.60 (m, 1H), 7.70 (m, 1H), 7.85 (m, 1H), 8.20 (br s, 1H, NH), 9.95 ppm (br s, 1H, OH); ^{13}C NMR (75 MHz, DMSO-*d*₆): δ 29.49 (CH₂), 31.06 (CH₂), 122.00 (CH), 123.39 (CH), 125.62 (CH), 126.05 (CH), 126.23 (2 × CH), 126.49 (CH), 128.56 (C), 134.03 (C), 134.18 (C), 171.27 (C=O), 174.39 (C=O) ppm. HRMS-ESI *m/z* [*M*-H]⁺ calcd for C₁₄H₁₂NO₃: 242.08172, found 242.08227.

4.2.2.5. *N*-5-Chloro-2-methylaniline-succinamic acid (116). Yield (1.42 g, 0.01 mmol) to yield the title compound as white powder (1.4 g, 70%): mp: 163–165 °C (cryst. diethylether); ν_{\max} (KBr): 3300–2650, 1701 cm^{-1} . ^1H NMR (300 MHz, DMSO-*d*₆): δ 2.14 (s, 3H, CH₃), 2.46 (m, 2H, CH₂), 2.57 (m, 2H, CH₂), 7.16 (m, 2H), 7.55 (m, 1H), 9.35 (br s, 1H, NH), 12.00 ppm (br s, 1H, OH) ppm; ^{13}C NMR (75 MHz, DMSO-*d*₆): δ 17.78 (CH₃), 29.38 (CH₂), 30.99 (CH₂), 124.21 (CH), 124.80 (CH), 130.15 (C), 132.22 (CH), 138.09 (C), 138.22 (C), 170.95 (C=O), 174.28 (C=O) ppm. HRMS-ESI *m/z* [*M*-H]⁺ calcd for C₁₁H₁₁ClNO₃: 240.04275, found 240.04329.

4.2.2.6. *N*-*p*-Anisidine-succinamic acid (117). Yield (1.4 g, 70%): mp: 167–170 °C (cryst. diethylether); ν_{\max} (KBr): 3300–2700, 1701 cm^{-1} . ^1H NMR (300 MHz, DMSO-*d*₆): δ 2.48 (m, 2H, CH₂), 3.01 (m, 2H, CH₂), 3.70 (s, 3H, OCH₃), 6.85 (m, 2H), 7.45 (m, 2H), 10.00 (br s, 1H, NH), 11.10 ppm (br s, 1H, OH) ppm; ^{13}C NMR (75 MHz, DMSO-*d*₆): δ 55.82 (OCH₃), 44.14 (CH₂), 46.18 (CH₂), 114.56 (2 × CH), 121.27 (2 × CH), 132.67 (C), 156.01 (C), 164.22 (C=O), 168.47 (C=O) ppm. HRMS-ESI *m/z* [*M*-H]⁺ calcd for C₁₁H₁₂NO₄: 222.07663, found 222.07718.

4.2.2.7. *N*-2-Chloroaniline-succinamic acid (118). Yield (1.4 g, 70%): mp: 145–148 °C (cryst. diethylether); ν_{\max} (KBr): 3300–2650, 1701 cm^{-1} . ^1H NMR (400 MHz, DMSO-*d*₆): δ 3.49 (m, 2H, CH₂), 3.61 (m, 2H, CH₂), 7.16 (m, 1H), 7.32 (m, 1H), 7.48 (m, 1H), 7.74 (m, 1H), 9.53 (br s, 1H, NH), 12.18 ppm (br s, 1H, OH) ppm; ^{13}C NMR (100 MHz, DMSO-*d*₆): δ 31.57 (CH₂), 33.26 (CH₂), 128.64 (CH), 128.83 (CH), 129.94 (CH), 130.04 (CH), 137.65 (C), 155.11 (C), 173.21 (C=O), 176.44 (C=O) ppm; HRMS-ESI *m/z* [*M*-H]⁺ calcd for C₁₀H₉ClNO₃: 226.02710, found 226.02722.

4.2.2.8. N-2-Aminopyridine-succinamic acid (119). Yield (1.4 g, 70%): mp: 134–137 °C. (cryst. diethylether); ν_{\max} (KBr): 3300–2650, 1701 cm^{-1} . ^1H NMR (400 MHz, DMSO- d_6): δ 2.81 (m, 2H, CH₂), 3.40 (m, 2H, CH₂), 6.56 (m, 1H), 6.94 (m, 1H), 7.19 (m, 1H), 7.47 (m, 1H), 9.93 (br s, 1H, NH), 12.16 (br s, 1H, OH) ppm; ^{13}C NMR (100 MHz, DMSO- d_6): δ 31.43 (CH₂), 32.46 (CH₂), 115.82 (CH), 128.53 (CH), 132.25 (CH), 140.18 (CH), 160.63 (C), 172.87 (C=O), 176.23 (C=O) ppm; HRMS-ESI m/z [$M-H$]⁺ calcd for C₉H₉N₂O₃: 193.06132, found 193.06187.

4.2.3. Preparation of *N,N*-di-oxalamide derivatives

To a magnetically stirred ice-bath cooled solution of the selected succinic monoamide derivative (4 mmol) in anhydrous dioxane (20 ml) neat oxalyl chloride was added (8 mmol). After stirring over 30 min the reaction mixture was warmed to room temperature. Two hours later, the reaction mixture was re-cooled to 0 °C in ice bath followed by drop wise addition of the particular aromatic amine (4 mmol) in pyridine (10 mL) to the reaction mixture. After stirring over 30 min the reaction mixture was warmed to room temperature and allowed to stir over 24 h. Subsequently, the reaction was carefully quenched with saturated sodium bicarbonate solution (200 mL). Finally, the mixture was filtered to offer the products as whitish to gray solids that were re-crystallized from acetone (see Scheme 2).

4.2.3.1. *N,N*-Di-*o*-tolyl-oxalamide (120). Prepared from **112** (1.0 g, 5 mmol) and commercially available *o*-toluidine (0.56 g, 5 mmol) to yield the title compound as faint off-white powder (0.3 g, 20%): mp: 208–210 °C (cryst. acetone); ν_{\max} (KBr): 3288, 1666 cm^{-1} ; ^1H NMR (400 MHz, DMSO- d_6): δ 2.30 (s, 6H, CH₃), 6.97 (m, 2H), 7.24 (m, 2H), 7.64 (m, 4H), 10.68 ppm (br s, 2H, NH) ppm; ^{13}C NMR (100 MHz, DMSO- d_6): δ 23.86 (2 × CH₃), 120.23 (2 × CH), 123.56 (2 × CH), 128.02 (2 × CH), 131.25 (2 × CH), 140.05 (2 × C), 140.66 (2 × C), 161.16 (2 × C=O) ppm. Anal. Calcd for C₁₆H₁₆N₂O₂: C, 71.62; H, 6.01; N, 10.44. Found: C, 68.50; H, 5.89; N, 9.95.

4.2.3.2. *N,N*-Di-*m*-tolyl-oxalamide (121). Prepared from **113** (1.0 g, 5 mmol) and commercially available *m*-toluidine (0.56 g, 5 mmol) to yield the title compound as faint off-white powder (0.35 g, 23%): mp: 132–135 °C (cryst. acetone); ν_{\max} (KBr): 3292, 1668 cm^{-1} ; ^1H NMR (400 MHz, DMSO- d_6): δ 2.30 (s, 6H, CH₃), 6.97 (m, 2H), 7.24 (m, 2H), 7.64 (m, 4H), 10.67 ppm (br s, 2H, NH) ppm; ^{13}C NMR (100 MHz, DMSO- d_6): δ 23.83 (2 × CH₃), 120.28 (2 × CH), 123.56 (2 × CH), 127.99 (2 × CH), 131.24 (2 × CH), 140.15 (2 × C), 140.63 (2 × C), 161.22 (2 × C=O) ppm. Anal. Calcd for C₁₆H₁₆N₂O₂: C, 71.62; H, 6.01. Found: C, 71.40; H, 6.87.

4.2.3.3. *N,N*'-Bis-(2-methoxy-4-methyl-phenyl)-oxalamide (122). Prepared from **113** (1.0 g, 4 mmol) and commercially available 4-methyl-*o*-anisidine (0.55 g, 4 mmol) to yield the title compound as faint off-white powder (0.3 g, 19%): mp: Decompose at 180 °C (cryst. acetone); ν_{\max} (KBr): 3361, 1687 cm^{-1} ; ^1H NMR (400 MHz, DMSO- d_6): δ 2.27 (s, 6H, CH₃), 3.87 (s, 6H, OCH₃), 7.01 (m, 4H), 8.00 (m, 2H), 9.80 ppm (br s, 2H, NH) ppm; ^{13}C NMR (100 MHz, DMSO- d_6): δ 23.16 (2 × CH₃), 58.76 (2 × OCH₃), 113.81 (2 × CH), 122.84 (2 × CH), 122.99 (2 × CH), 128.47 (2 × C), 132.20 (2 × C), 149.57 (2 × C), 159.68 (2 × C=O) ppm; HRMS-ESI m/z [$M+Na$]⁺ calcd for C₁₈H₂₀N₂NaO₄: 351.13207, found 351.13152.

4.2.3.4. *N*-(5-Chloro-2-methyl-phenyl)-*N*'-naphthalen-1-yl-oxalamide (123). Prepared from **116** (1.0 g, 4 mmol) and commercially available 1-naphthylamine (0.60 g, 4 mmol) to yield the title compound as faint off-white powder (0.2 g, 13%): mp: 162–165 °C (cryst. acetone); ν_{\max} (KBr): 3276, 1674, 1666 cm^{-1} ; ^1H

NMR (400 MHz, DMSO- d_6): δ 2.26 (s, 3H, CH₃), 7.31 (m, 2H), 7.66 (m, 5H), 7.94 (m, 3H), 10.40 (br s, 1H, NH), 11.0 (br s, 1H, NH) ppm; ^{13}C NMR (100 MHz, DMSO- d_6): δ 19.76 (CH₃), 125.60 (CH), 126.93 (CH), 128.16 (2 × CH), 128.52 (CH), 128.89 (2 × CH), 129.47 (CH), 130.79 (CH), 131.00 (C), 132.71 (CH), 133.84 (C), 134.61 (C), 134.96 (C), 136.34 (C), 139.06 (C), 161.32 (C=O), 161.91 (C=O) ppm; HRMS-ESI m/z [$M-H$]⁺ calcd for C₁₉H₁₄ClN₂O₂: 337.07438, found 337.07493. Anal. Calcd for C₁₉H₁₅ClN₂O₂: C, 67.36; H, 4.46; N, 8.27. Found: C, 68.28; H, 4.52; N, 8.19.

4.2.3.5. *N*-Naphthalen-1-yl-*N*'-o-tolyl-oxalamide (124). Prepared from **115** (1.0 g, 4 mmol) and commercially available *o*-toluidine (0.44 g, 4 mmol) to yield the title compound as faint off-white powder (0.3 g, 21%): mp: 125–129 °C (cryst. acetone); ν_{\max} (KBr): 3280, 1666, 1585 cm^{-1} ; ^1H NMR (400 MHz, DMSO- d_6): δ 2.25 (s, 3H, CH₃), 7.24 (m, 4H), 7.56 (m, 4H), 7.88 (m, 3H), 10.30 (br s, 1H, NH), 10.90 (br s, 1H, NH) ppm; ^{13}C NMR (100 MHz, DMSO- d_6): δ 20.25 (CH₃), 125.94 (CH), 125.63 (CH), 127.39 (CH), 127.50 (CH), 128.19 (CH), 128.87 (CH), 129.40 (CH), 130.80 (CH), 130.99 (CH), 133.10 (CH), 134.84 (CH), 134.92 (C), 135.07 (C), 136.34 (C), 137.67 (C), 137.75 (C), 161.18 (C=O), 162.23 (C=O) ppm. Anal. Calcd for C₁₉H₁₆N₂O₂: C, 74.98; H, 5.30; N, 9.20. Found: C, 72.06; H, 5.41; N, 9.16.

4.2.3.6. *N*-(2-Methoxy-phenyl)-*N*'-naphthalen-1-yl-oxalamide (125). Prepared from **115** (1.0 g, 4 mmol) and commercially available *o*-anisidine (0.51 g, 4 mmol) to yield the title compound as faint off-white powder (0.25 g, 17%): mp: 176–179 °C (cryst. acetone); ν_{\max} (KBr): 3344, 3303, 1678, 1668 cm^{-1} ; ^1H NMR (400 MHz, DMSO- d_6): δ 3.90 (s, 3H, OCH₃), 7.18 (m, 3H), 7.57 (m, 4H), 7.91 (m, 3H), 8.27 (m, 1H), 9.88 ppm (br s, 1H, NH), 11.05 (br s, 1H, NH) ppm; ^{13}C NMR (100 MHz, DMSO- d_6): δ 58.68 (OCH₃), 113.93 (CH), 122.15 (CH), 122.29 (CH), 123.36 (CH), 125.64 (CH), 125.92 (C), 128.14 (2 × CH), 128.37 (C), 128.92 (2 × CH), 129.60 (CH), 130.75 (CH), 131.06 (C), 134.96 (C), 136.32 (C), 151.64 (C=O), 160.00 (C=O) ppm; HRMS-ESI m/z [$M+Na$]⁺ calcd for C₁₉H₁₆N₂NaO₃: 43.10586, found 343.11188. Anal. Calcd for C₁₉H₁₆N₂O₃: C, 71.24; H, 5.03; N, 8.74. Found: C, 70.96; H, 5.20; N, 8.75.

4.2.3.7. *N*-(2-Methoxy-4-methyl-phenyl)-*N*'-naphthalen-1-yl-oxalamide (126). Prepared from **115** (1.0 g, 4 mmol) and commercially available 4-methyl-*o*-anisidine (0.55 g, 4 mmol) to yield the title compound as faint off-white powder (0.35 g, 23%): mp: 160–162 °C (cryst. acetone); ν_{\max} (KBr): 3357, 1699, 1682 cm^{-1} ; ^1H NMR (400 MHz, DMSO- d_6): δ 2.26 (s, 3H, CH₃), 3.86 (s, 3H, OCH₃), 7.00 (m, 2H), 7.57 (m, 4H), 7.91 (m, 2H), 7.97 (m, 1H), 8.10 (s, 1H), 9.80 (br s, 1H, NH), 11.0 (br s, 1H, NH) ppm; ^{13}C NMR (100 MHz, DMSO- d_6): δ 23.23 (CH₃), 58.69 (OCH₃), 113.73 (CH), 122.72 (CH), 125.51 (CH), 125.78 (CH), 127.96 (C), 128.16 (CH), 128.25 (CH), 128.96 (2 × CH), 129.61 (CH), 130.79 (CH), 130.98 (C), 132.19 (C), 134.74 (C), 136.31 (C), 149.49 (C), 159.74 (C=O), 161.92 (C=O) ppm; HRMS-ESI m/z [$M+Na$]⁺ calcd for C₂₀H₁₈N₂NaO₃: 357.12151, found 357.12096. Anal. Calcd for C₂₀H₁₈N₂O₃: C, 71.84; H, 5.43; N, 8.38. Found: C, 69.61; H, 5.55; N, 8.34.

4.2.3.8. *N*-Naphthalen-1-yl-*N*'-p-tolyl-oxalamide (127). Prepared from **115** (1.0 g, 4 mmol) and commercially available *p*-toluidine (0.44 g, 4 mmol) to yield the title compound as faint off-white powder (0.2 g, 14%): mp: 166–170 °C (cryst. acetone); ν_{\max} (KBr): 3340, 3302, 1703, 1674 cm^{-1} ; ^1H NMR (300 MHz, DMSO- d_6): δ 2.26 (s, 3H, CH₃), 7.58 (m, 1H), 7.65 (m, 4H), 7.76 (m, 2H), 7.87 (m, 4H), 10.75 (br s, 1H, NH), 10.93 (br s, 1H, NH) ppm; ^{13}C NMR (75 MHz, DMSO- d_6): δ 21.06 (CH₃), 120.93 (CH), 123.44 (CH), 123.56 (CH), 123.63 (CH), 126.06 (CH), 126.72 (2 × CH), 126.77 (CH), 127.24 (CH), 128.63 (CH), 128.91 (2 × C),

129.66 (CH), 133.02 (C), 134.20 (C), 135.69 (C), 158.93 (C=O), 160.21 (C=O) ppm. Anal. Calcd for $C_{19}H_{16}N_2O_2$: C, 74.98; H, 5.30; N, 9.20. Found: C, 71.35; H, 5.07; N, 8.83.

4.2.3.9. N-Naphthalen-1-yl-N'-m-tolyl-oxalamide (128). Prepared from **115** (1.0 g, 4 mmol) and commercially available *m*-toluidine (0.44 g, 4 mmol) to yield the title compound as faint off-white powder (0.25 g, 17%): mp: 127–130 °C (cryst. acetone); ν_{\max} (KBr): 3340, 3265, 1687, 1666 cm^{-1} ; 1H NMR (300 MHz, DMSO- d_6): δ 2.28 (s, 3H, CH₃), 7.58 (m, 1H), 7.65 (m, 4H), 7.76 (m, 2H), 7.87 (m, 4H), 10.75 (br s, 1H, NH), 10.93 (br s, 1H, NH) ppm; ^{13}C NMR (75 MHz, DMSO- d_6): δ 21.73 (CH₃), 117.97 (CH), 118.06 (CH), 121.30 (CH), 123.31 (CH), 125.80 (CH), 126.01 (CH), 126.71 (CH), 126.75 (CH), 127.20 (CH), 128.60 (CH), 128.80 (C), 129.07 (CH), 132.80 (C), 134.17 (C), 137.90 (C), 138.49 (C), 158.95 (C=O), 160.26 (C=O) ppm. Anal. Calcd for $C_{19}H_{16}N_2O_2$: C, 74.98; H, 5.30; N, 9.20. Found: C, 72.65; H, 5.47; N, 9.61.

4.2.3.10. N-(5-Chloro-2-methyl-phenyl)-N'-(2-methoxy-4-methyl-phenyl)-oxalamide (129). Prepared from **116** (1.0 g, 4 mmol) and commercially available 4-methyl-*o*-anisidine (0.057 g, 4 mmol) to yield the title compound as faint off-white powder (0.35 g, 22%): mp: 160–163 °C (cryst. acetone); ν_{\max} (KBr): 3361, 1687 cm^{-1} ; 1H NMR (400 MHz, DMSO- d_6): δ 2.26 (s, 6H, 2 × CH₃), 3.87 (s, 3H, OCH₃), 7.00 (m, 3H), 8.00 (s, 3H), 9.81 (br s, 1H, NH), 9.91 (br s, 1H, NH) ppm; ^{13}C NMR (100 MHz, DMSO- d_6): δ 22.24 (2 × CH₃), 57.84 (OCH₃), 112.73 (CH), 112.81 (CH), 113.73 (CH), 116.52 (CH), 121.96 (CH), 122.52 (CH), 127.59 (C), 128.73 (C), 130.68 (C), 131.77 (C), 132.17 (C), 149.32 (C), 159.16 (C=O), 161.56 (C=O) ppm; HRMS-ESI m/z [$M+Na$]⁺ calcd for $C_{17}H_{17}ClN_2NaO_3$: 355.08254, found 355.08199.

4.2.3.11. N-(2-Methoxy-4-methyl-phenyl)-N'-(4-methoxy-phenyl)-oxalamide (130). Prepared from **117** (1.0 g, 4 mmol) and commercially available 4-methyl-*o*-anisidine (0.058 g, 4 mmol) to yield the title compound as faint off-white powder (0.30 g, 19%): mp: 152–156 °C (cryst. acetone); ν_{\max} (KBr): 3334, 3302, 1666, 1660 cm^{-1} ; 1H NMR (400 MHz, DMSO- d_6): δ 2.27 (s, 3H, CH₃), 3.74 (s, 3H, OCH₃), 3.86 (s, 3H, OCH₃), 6.98 (m, 4H), 7.75 (m, 2H), 8.02 (m, 1H), 9.84 ppm (br s, 1H, NH), 10.08 ppm (br s, 1H, NH) ppm; ^{13}C NMR (100 MHz, DMSO- d_6): δ 23.24 (CH₃), 57.87 (OCH₃), 58.71 (OCH₃), 113.73 (CH), 116.52 (2 × CH), 122.59 (C), 122.73 (CH), 124.68 (CH), 124.77 (2 × CH), 128.17 (C), 132.12 (C), 133.10 (C), 149.55 (C), 158.96 (C=O), 160.42 (C=O) ppm. Anal. Calcd for $C_{17}H_{18}N_2O_4$: C, 64.96; H, 5.77; N, 8.91. Found: C, 63.02; H, 5.57; N, 8.43.

4.2.3.12. N-Benzyl-N'-(2-chloro-phenyl)-oxalamide (131). Prepared from **118** (1.0 g, 4 mmol) and commercially available benzylamine (0.47 g, 4 mmol) to yield the title compound as faint off-white powder (0.30 g, 20%): mp: 139–143 °C (cryst. water); ν_{\max} (KBr): 3286, 1668, 1655 cm^{-1} ; 1H NMR (400 MHz, DMSO- d_6): δ 4.4 (2H, CH₂), 7.23 (m, 2H), 7.31 (m, 4H), 7.40 (m, 1H), 7.55 (m, 1H), 8.00 (m, 1H), 9.70 (br s, 1H, NH), 10.16 (br s, 1H, NH) ppm; ^{13}C NMR (100 MHz, DMSO- d_6): δ 45.44 (CH₂), 126.26 (CH), 126.50 (CH), 129.49 (CH), 129.70 (CH), 130.15 (2 × CH), 130.58 (2 × CH), 130.99 (CH), 132.21 (C), 136.17 (C), 141.0 (C), 160.73 (C=O), 162.20 (C=O) ppm. Anal. Calcd for $C_{15}H_{13}ClN_2O_2$: C, 62.40; H, 4.52; N, 9.70. Found: C, 62.59; H, 4.46; N, 9.78.

4.2.3.13. N-(2-Methoxy-phenyl)-N'-pyridin-2-yl-oxalamide (132). Prepared from **119** (1.0 g, 5 mmol) and commercially available *o*-anisidine (0.63 g, 5 mmol) to yield the title compound as faint off-white powder (0.35 g, 21%): mp: 132–136 °C (cryst. water); ν_{\max} (KBr): 3383, 3357, 1716, 1691 cm^{-1} ; 1H NMR (400 MHz, acetone- d_6): δ 4.00 (s, 3H, OCH₃), 7.07 (m, 1H), 7.27

(m, 3H), 7.96 (m, 1H), 8.27 (m, 1H), 8.42 (m, 2H), 9.86 (br s, 1H, NH), 10.27 (br s, 1H, NH) ppm; ^{13}C NMR (100 MHz, DMSO- d_6): δ 57.83 (OCH₃), 113.0 (CH), 115.69 (2 × CH), 121.47 (CH), 122.94 (CH), 123.12 (2 × CH), 127.60 (CH), 132.71 (CH), 135.21 (C), 136.17 (C), 141.0 (C), 161.26 (C=O), 164.58 (C=O) ppm; HRMS-ESI m/z [$M+Na$]⁺ calcd for $C_{14}H_{13}N_3O_3$: 272.10352, found 272.10297. Anal. Calcd for $C_{14}H_{13}N_3O_3$: C, 61.99; H, 4.83; N, 15.49. Found: C, 60.77; H, 4.77; N, 14.79.

4.3. In vitro experimental studies

4.3.1. Chemicals of bioassay

Materials were purchased from corresponding companies and were used in the experimentation without further purification. GPa rabbit enzyme, dimethyl sulfoxide (DMSO), Hepes buffer, Glucose-1-phosphate, glycogen, magnesium chloride, KCl, malachite green, ammonium molybdate, EGTA. All were obtained from (Sigma–Aldrich, USA). NCI hit were kindly donated by the National Cancer Institute.

4.3.2. In vitro GP enzyme inhibition assay

GPa (from rabbit muscle), glycogen, glucose-1-phosphate, malachite green, and ammonium molybdate were purchased from the Sigma–Aldrich Corporation (St. Louis, MO, USA). Reagents and solvents were obtained from commercial suppliers and used without further purification.

The enzymatic inhibition of phosphorylase activity was monitored using microplate reader (BioTek, USA) based on published methods.⁴ In brief, GPa activity was measured in the direction of glycogen synthesis by the release of phosphate from glucose-1-phosphate. Each compound was dissolved in DMSO and diluted appropriately. The enzyme was added to the 100 μ L buffer containing 50 mM Hepes (pH 7.2), 100 mM KCl, 2.5 mM MgCl₂, 0.5 mM glucose-1-phosphate, and 1 mg/mL glycogen together with tested compounds in 96-well microplates. After the addition of 150 μ L of 1 M HCl containing 10 mg/mL ammonium molybdate and 0.38 mg/mL malachite green, reactions were run at 22 °C for 20 min, then the phosphate absorbance was measured at 620 nm. Caffeine was used as a standard inhibitor for GP enzyme.⁶⁸

Acknowledgments

This project was partially sponsored by the Faculty of Graduate Studies (This work is part of Ph.D. Thesis of Rand Shahin). The authors thank the Deanship of Scientific Research and Hamdi-Mango Center for Scientific Research at the University of Jordan for their generous funds.

Supplementary data

Supplementary data associated with this article can be found, in the online version, at doi:10.1016/j.bmc.2011.06.086.

References and notes

- (a) Ercan-Fang, N.; Taylor, R. M.; Treadway, L. J.; Levy, B. C.; Genereux, E. P.; Gibbs, M. E.; Rath, L. V.; Kwon, Y.; Gannon, C. M.; Nuttall, Q. F. *Am. J. Physiol. Endocrinol. Metab.* **2005**, 289, E366; (b) Praly, J.-P.; Vidal, S. *Mini-Rev. Med. Chem.* **2010**, 10, 1102; (c) Hayes, J. M.; Leonidas, D. D. *Mini-Rev. Med. Chem.* **2010**, 10, 1156.
- Tsirkone, V. G.; Tsoukala, E.; Lamprakos, C.; Manta, S.; Hayes, J. M.; Skamnaki, V. T.; Drakou, C.; Zographos, S. E.; Komiotis, D.; Leonidas, D. D. *Bioorg. Med. Chem.* **2010**, 15, 3413.
- Oikonomakos, N. G. *Curr. Protein Pept. Sci.* **2002**, 3, 561.
- Martin, W. H.; Hoover, D. J.; Armento, S. J.; Stock, I. A.; McPherson, R. K.; Danley, D. E.; Stevenson, R. W.; Barrett, E. J.; Treadway, J. L. *Proc. Natl. Acad. Sci. U.S.A.* **1998**, 95, 1776.
- (a) Deng, Q.; Lu, Z.; Bohn, J.; Ellsworth, K. P.; Myers, R. W.; Geissler, W. M.; Harris, G.; Willoughby, C. A.; Chapman, K.; McKeever, B.; Mosley, R. J. *Mol.*

- Graphics Modell. **2005**, *23*, 457; (b) Oikonomakos, N. G.; Somsak, L. *Curr. Opin. Investig. Drugs* **2008**, *9*, 379; (c) Somsak, L.; Czifrak, K.; Toth, M.; Bokor, E.; Chrykina, E. D.; Alexacou, K. M.; Hayes, J. M.; Tiraidis, C.; Lazoura, E.; Leonidas, D. D.; Zographos, S. E.; Oikonomakos, N. G. *Curr. Med. Chem.* **2008**, *15*, 2933; (d) Henke, B. R.; Sparks, S. M. *Mini-Rev. Med. Chem.* **2006**, *6*, 845.
6. Zographos, S. E.; Oikonomakos, N. G.; Tsitsanou, K. E.; Leonidas, D. D.; Chrykina, E. D.; Skamnaki, V. T.; Bischoff, H.; Goldmann, S.; Watson, K. A.; Johnson, L. N. *Structure* **1997**, *5*, 1413.
 7. Agius, L. *Mini-Rev. Med. Chem.* **2010**, *10*, 1175.
 8. Chen, L.; Li, H.; Liu, J.; Zhang, L.; Liu, H.; Jiang, H. *Bioorg. Med. Chem.* **2007**, *15*, 6763.
 9. (a) Chen, J.; Liu, J.; Zhang, L. Y.; Wu, G.; Hua, W.; Wu, X.; Sun, H. *Bioorg. Med. Chem. Lett.* **2006**, *16*, 2915; (b) Bradley, S. E.; Jeevaratnam, R. P.; Krulle, T. M.; Procter, M. J.; Rowley, R. J.; Thomas, G. H.; Valdes, W02005085245, 2005.
 10. Prathipati, P.; Pandey, G.; Saxena, K. A. *J. Chem. Inf. Model.* **2005**, *45*, 136.
 11. Gohlke, H.; Klebe, G. *J. Med. Chem.* **2002**, *45*, 4153.
 12. Sutherland, J. J.; Nandigam, R. K.; Erickson, J. A.; Vieth, M. *J. Chem. Inform. Model.* **2007**, *47*, 2293.
 13. Evans, K. A.; Li, Y. H.; Coppo, F. T.; Graybill, T. L.; Cichy-Knight, M.; Patel, M.; Gale, J.; Li, H.; Thrall, S. H.; Tew, D.; Tavares, F.; Thomson, S. A.; Weiel, E. J.; Boucheron, J. A.; Clancy, D. C.; Epperly, A. H.; Golden, P. L. *Bioorg. Med. Chem. Lett.* **2008**, *18*, 4068.
 14. Peng, Z.; Zhiliang, L. *Sci. China, Ser. B* **2007**, *50*, 568.
 15. Beeley, N. R. A.; Sage, C. *Targets* **2003**, *2*, 19.
 16. Klebe, G. *Drug Discovery Today* **2006**, *11*, 580.
 17. Steuber, H.; Zentgraf, M.; Gerlach, C.; Sottriffer, C. A.; Heine, A.; Klebe, G. *J. Mol. Biol.* **2006**, *363*, 174.
 18. Stubbs, M. T.; Reyda, S.; Dullweber, F.; Moller, M.; Klebe, G.; Dorsch, D.; Mederski, W.; Wurziger, H. *ChemBioChem* **2002**, *3*, 246.
 19. DePristo, M. A.; de Bakker, P. I. W.; Blundell, T. L. *Structure* **2004**, *12*, 831.
 20. Taha, M. O.; Bustanji, Y.; Al-Ghoussein, M. A. S.; Mohammad, M.; Zalloum, H.; Al-Masri, I. M.; Atallah, N. *J. Med. Chem.* **2007**, *51*, 2062.
 21. Taha, M. O.; Atallah, N.; Al-Bakri, A. G.; Paradis-Bleau, C.; Zalloum, H.; Younis, K.; Levesque, R. C. *Bioorg. Med. Chem.* **2008**, *16*, 1218.
 22. Taha, M. O.; Bustanji, Y.; Al-Bakri, A. G.; Yousef, M.; Zalloum, W. A.; Al-Masri, I. M.; Atallah, N. *J. Mol. Graphics Modell.* **2007**, *25*, 870.
 23. Al-masri, I. M.; Mohammad, M. K.; Taha, M. O. *Chem. Med. Chem.* **2008**, *3*, 1763.
 24. Taha, M. O.; Dahabiyeh, L. A.; Bustanji, Y.; Zalloum, H.; Saleh, S. *J. Med. Chem.* **2008**, *51*, 6478.
 25. Al-Nadaf, A.; Abu Sheikha, G.; Taha, M. O. *Bioorg. Med. Chem.* **2010**, *18*, 3088.
 26. Abu-Hammad, A.; Zalloum, W. A.; Zalloum, H.; Abu-Sheikha, G.; Taha, M. O. *Eur. J. Med. Chem.* **2009**, *44*, 2583.
 27. Abu Khalaf, R.; Abu Sheikha, G.; Bustanji, Y.; Taha, M. O. *Eur. J. Med. Chem.* **2010**, *45*, 1598.
 28. Al-Sha'er, M. A.; Taha, M. O. *Eur. J. Med. Chem.* **2010**, *45*, 4316.
 29. Abdula, A.; Abu Khalaf, R.; Mubarak, M.; Taha, M. *J. Comput. Chem.* **2010**, *26*, 463.
 30. Al-Sha'er, M. A.; Taha, M. O. *J. Chem. Info. Model.* **2010**, *50*, 1706.
 31. Singh, J.; Chuaqui, C.; Sjodin, P.; Lee, W.; Pontz, T.; Corbley, M.; Cheung, H.; Arduini, R.; Mead, J.; Newman, M.; Papadatos, J.; Bowes, S.; Josiah, S.; Ling, L. *Bioorg. Med. Chem. Lett.* **2003**, *13*, 4355.
 32. Taha, M. O.; Qandil, A. M.; Zaki, D. D.; Aldamen, M. A. *Eur. J. Med. Chem.* **2005**, *40*, 701.
 33. Garino, C.; Tomita, T.; Pietrancosta, N.; Laras, Y.; Rosas, R.; Herbet, G.; Maigret, B.; Quéléver, G.; Iwatsubo, T.; Kraus, J. *J. Med. Chem.* **2006**, *49*, 4275.
 34. Rosauer, K. G.; Ogawa, A. K.; Willoughby, C. A.; Ellsworth, K. P.; Geissler, W. M.; Myers, W. R.; Chapman, K. T.; Harris, G.; Moller, D. E. *Bioorg. Med. Chem.* **2003**, *13*, 4385.
 35. CATALYST 4.11 Users' Manual; Ligandfit, 2005.
 36. Sheridan, R. P.; Kearsley, S. K. *Drug Discovery Today* **2002**, *7*, 903.
 37. CATALYST 4.11 Users' Manual; Accelrys Software Inc.: San Diego, CA, 2005.
 38. Kurogi, Y.; Güner, O. F. *Curr. Med. Chem.* **2001**, *8*, 1035.
 39. Li, H.; Sutter, J.; Hoffmann, R. In *Pharmacophore Perception, Development, and Use in Drug Design*; Güner, O. F., Ed.; International University Line: La Jolla, CA, 2000; p 173.
 40. Poptodorov, K.; Luu, T.; Langer, T.; Hoffmann, R. In *Methods and Principles in Medicinal Chemistry. Pharmacophores and Pharmacophores Searches*; Hoffmann, R. D., Ed.; Wiley-VCH: Weinheim, Germany, 2006; Vol. 2, pp 17–47.
 41. Sutter, J.; Güner, O.; Hoffmann, R.; Li, H.; Waldman, M. In *Pharmacophore Perception, Development, and Use in Drug Design*; Güner, O. F., Ed.; International University Line: La Jolla, CA, 2000; p 501.
 42. Bersuker, I. B.; Bahçeci, S.; Boggs, J. E. In *Pharmacophore Perception, Development, and Use in Drug Design*; Güner, O. F., Ed.; International University Line: La Jolla, CA, 2000; p 457.
 43. Fisher, R. *The Principle of Experimentation Illustrated by a Psycho-Physical ExpeHafner Publishing Co*, 8th ed.; Hafner Publishing: New York, 1966.
 44. CERUS2, QSAR Users' Manual, version 4.10; Accelrys Inc.: San Diego, CA, 2005, pp 43–88, 221–235.
 45. Ramsey, L. F.; Schafer, W. D. *The Statistical Sleuth*, 1st ed.; Wadsworth Publishing Company: Belmont, CA, 1997.
 46. Sprague, P. W.; Hoffmann, R.; Van de Waterbeemd, H.; Testa, B.; Folkers, G. *Curr. Tools Med. Chem.* **1997**, *230*.
 47. Lipinski, C. A.; Lombardo, F.; Dominy, B. W.; Feeney, P. J. *Adv. Drug Delivery Rev.* **2001**, *46*, 3.
 48. Veber, D. F.; Johnson, S. R.; Cheng, H. Y.; Smith, B. R.; Ward, K. W.; Kopple, K. D. *Bioorg. Med. Chem.* **2002**, *45*, 2615.
 49. Mai, A.; Cheng, D.; Bedford, M. T.; Valente, S.; Nebbioso, A.; Perrone, A.; Brosch, G.; Sbardella, G.; Bellis, F. D.; Miceli, M.; Altucci, L. *J. Med. Chem.* **2008**, *51*, 2279.
 50. Gerhard, B. V.; Rene, M. L. *J. Chem. Soc. 1: Org. Bio-Org. Chem.* **1978**, *11*, 1338.
 51. Jain, A. N. *J. Comput. Aided Mol. Des.* **1996**, *10*, 427.
 52. Venkatachalam, C. M.; Jiang, X.; Oldfield, T.; Waldman, M. *J. Mol. Graphics Modell.* **2003**, *21*, 289.
 53. Krammer, A.; Kirchhoff, P. D.; Jiang, X.; Venkatachalam, C. M.; Waldman, M. *J. Mol. Graphics Modell.* **2005**, *23*, 395.
 54. Gehlhaar, D. K.; Verkhivker, G. M.; Rejto, P. A.; Sherman, C. J.; Fogel, D. B.; Fogel, L. J.; Freer, S. T. *Chem. Biol.* **1995**, *2*, 317.
 55. Gehlhaar, D. K.; Bouzida, D.; Rejto, P. A. In *Rational Drug Design: Novel Methodology and Practical Applications*; Parrill, L.; Reddy, M. R., Eds.; American Chemical Society: Washington, DC, 1999; pp 292–311.
 56. Muegge, I.; Martin, Y. C. *J. Med. Chem.* **1999**, *42*, 791.
 57. Muegge, I. *Perspect. Drug Discovery Des.* **2000**, *20*, 99.
 58. Muegge, I. *J. Comput. Chem.* **2001**, *22*, 418.
 59. Bemis, G. W.; Murcko, M. A. *J. Med. Chem.* **1996**, *39*, 2887.
 60. Discovery Studio 2.5.5 User Guide, 2010.
 61. Krovat, E. M.; Langer, T. *J. Chem. Inf. Comput. Sci.* **2004**, *44*, 1123.
 62. Kirchmair, J.; Markt, P.; Distinto, S.; Wolber, G.; Langer, T. *J. Comput. Aided Mol. Des.* **2008**, *22*, 213.
 63. Verdonk, M. L.; Marcel, L.; Berdini, V.; Hartshorn, M. J.; Mooij, W. T. M.; Murray, C. W.; Taylor, R. D.; Watson, P. *J. Chem. Inform. Comput. Sci.* **2004**, *44*, 793.
 64. Irwin, J. J.; Shoichet, B. K. *J. Chem. Inf. Comput. Sci.* **2005**, *45*, 177.
 65. Triballeau, N.; Acher, F.; Brabet, I.; Pin, J.-P.; Bertrand, H.-O. *J. Med. Chem.* **2005**, *48*, 2534.
 66. Gao, H.; Williams, C.; Labute, P.; Bajorath, J. *J. Chem. Inf. Comput. Sci.* **1999**, *39*, 164.
 67. Jacobsson, M.; Liden, P.; Stjernschantz, E.; Bostroem, H.; Norinder, U. *J. Med. Chem.* **2003**, *46*, 5781.
 68. Loughlin, A. W.; Pierens, K. G.; Petersson, J. M.; Henderson, C. L.; Healy, C. P. *Bioorg. Med. Chem.* **2008**, *16*, 6172.
 69. Birch, A. M.; Kenny, P. W.; Oikonomakos, N. G.; Otterbein, L.; Schofield, P.; Paul, R. O.; Whittamore, Whalley, D. P. *Bioorg. Med. Chem. Lett.* **2007**, *17*, 394.
 70. Georgiyants, V. A. *Klinichna Farmatsiya* **2003**, *7*, 63.
 71. Georgiyants, V. A.; Bezuglyi, P. A. *Russ. J. Org. Chem.* **2002**, *38*, 1079.
 72. Shahnawaz, M.; Naqi, A.; Rao, A. V.; Seth, D. S. *Orient. J. Chem.* **2008**, *24*, 701.
 73. Moradi, R.; Enayat, O. *Chin. Chem. Lett.* **2010**, *21*, 542.
 74. Pelly, S. C.; Parkinson, C. J.; Van Otterlo, W. A. L.; De Koning, C. B. *J. Org. Chem.* **2005**, *70*, 10474.
 75. Kubicova, L.; Waisser, K.; Kunes, J.; Kralova, K.; Odlernova, Z.; Slosarek, M.; Janota, J.; Svoboda, Z. *Molecules* **2000**, *5*, 714.
 76. Biland, Hans R.; Duennenberger, M.; Luethi, C. *Oxalic Acid Diarylamides*. U.S., 1975, p 31.
 77. CIBA-GEIGY, 1968.
 78. Goldfarb, D.S. U.S. Pat. Appl. Publ., 2009, 57.